NUMERICAL ANALYSIS OF BASIC MICROSTRIP ANTENNA STRUCTURES USING THE MOMENT METHOD

by

YIYU LIN

A thesis
presented to the University of Manitoba
in partial fulfillment of the
requirements for the degree of
Master of Science
in
the Department of Electric Engineering

Winnipeg, Manitoba, 1984

NUMERICAL ANALYSIS OF BASIC MICROSTRIP ANTENNA STRUCTURES USING THE MOMENT METHOD

BY

YIYU LIN

A thesis submitted to the Faculty of Graduate Studies of the University of Manitoba in partial fulfillment of the requirements of the degree of

MASTER OF SCIENCE

ABSTRACT

Integral equations for both interior and exterior fields of microstrip antennas are formulated in terms of the tangential electric and magnetic field distributions over the conducting patch and dielectric substrate surfaces. The boundary conditions on the conducting patch and the dielectric surface are applied and a set of integral equations for the above surface distributions are obtained. It is shown that using a moment method, these integral equations can be reduced to a matrix equation, a solution of which gives the required surface field distributions. The method is then applied to both square and rectangular microstrip patch antennas and the computed radiation patterns are compared with the experimentally determined results to investigate the convergence and accuracy of the numerically obtained data. Based on these investigations the usefulness of the method as an accurate tool for studying microstrip antennas is then pointed out.

ACKNOWLEDGMENTS

The author wishes to express his sincere appreciation to Prof. L. Shafai of the Electrical Engineering Department, University of Manitoba, for his guidance, constant encouragement and constructive criticism, throughout all phases of this work.

It is a pleasure to thank Prof. E. Bridges, Prof. F. Arscott and Prof. A. Trim for their many helpful suggestions. The author is also indebted to Mr. A. McKay, Electronics Technologist, Mr. A. Symmons, Machining Technologist and B. Tabachinick, Antenna Technologist of the Electrical Engineering Department who have made various contributions in the fabrication process of the antenna model.

The financial support by the National Research Council of Canada in the form of Research Assistantship and also through the University of Manitoba in the form of University Fellowship are appreciated.

CONTENTS

ABSTRACT ii

ACKNOWLEDGMENTS iii

Chapter page

I. INTRODUCTION 1

II. THEORY 7

2. 1 Introduction 7
2. 2 Electromagnetic Field Integral Equations 8
2. 3 Surface Integral Equations and Singularities . . 11
2. 3. 1 Surface Integral Equations 12
2. 3. 2 Singularities 14
2. 4 Equations for Microstrip Patch Antenna 21
2. 4. 1 Interior Fields 23
2. 4. 2 Exterior Fields 24
2. 4. 3 Coupled Integral Equations 25

III. NUMERICAL MODELING 29

3. 1 Introduction 29
3. 2 The General Method 30
3. 3 Application of the Method 32
3. 3. 1 Centrally Fed Square Patch 32
3. 3. 2 The Excitation Source 41
3. 4 Radiation Pattern and the Input Impedance . . . 44
3. 4. 1 Radiation Pattern 44
3. 4. 2 The Input Impedance 47

IV. RESULTS AND DISCUSSION 49

4. 1 Field Distribution 50
4. 2 Comparison of Computed and Measured Radiation Patterns 56
4. 3 Comparison with Transmission Line Modeling . . . 65
4. 4 Effect of Surface Segmentation 72

V. CONCLUSION 81

Appendix page

A. THE DERIVATION OF EQUATIONS (3.12) - (3.15) 82

B. THE ENTRIES OF THE COEFFICIENT MATRIX 88

C. RADIATION PATTERNS OF AIR FILLED DISK PATCH ANTENNA 94

REFFERENCES 98

LIST OF FIGURES

Figure		page
2.1.	A Current Element at the Coordinate Origin	8
2.2.	The Surfaces in the Derivation of the Integral Equations	12
2.3.	The Definition of Tangential Principal Area Vector T	16
2.4.	The Regular Principal Area for The Singular Point	17
2.5.	The Arbitrary Principal Area For the Singular Point	19
2.6.	The Microstrip Patch Antenna	21
2.7.	The Integral Regions over the Antenna	22
3.1.	The Centrally Fed Patch	33
3.2.	The Unknown Fields on the Surface	34
3.3.	The Segmentation of the Whole Antenna	37
3.4.	The Relationship of the Real and Image Field Vector	39
3.5.	The Current Source Excitation	43
3.6.	Geometry for Evaluating the Radiation Field . . .	45
3.7.	Conventional Coordinate Orientation	46
4.1.	Geometry and Segmentation for Field Distributions	51
4.2.	Field distributions for $x = 0.2542\,\lambda_g$	52
4.3.	Field Distributions for $x = -0.2542\,\lambda_g$	53
4.4.	Field Distributions for $y = \pm 0.2542\,\lambda_g$	54

4.5. Field Distributions for $y = \pm 0.00417\,\lambda_g$ 55
4.6. Investigated Antenna Segmentations 58
4.7. 59
4.8. 60
4.9. 61
4.10. 62
4.11. 63
4.12. 64
4.13. 66
4.14. 67
4.15. 68
4.16. 69
4.17. 70
4.18. 71
4.19. 73
4.20. 74
4.21. 75
4.22. 76
4.23. 79
4.24. 80
C.1. The Geometry of the Disk Antenna 95
C.2. 96
C.3. 97

Chapter I

INTRODUCTION

Since the 1970's, the popularity of microstrip antennas has increased because of their geometric properties that allow the antenna to be mounted on vehicles, aircraft, missiles, and satellites. This increased use has aroused intense interest among antenna theoreticians and engineers in both the analytical and practical aspects of microstrip antenna design. Considerable effort has been put into investigating the radiating mechanism and analysing the general characteristics of basic microstrip radiating elements. The purpose of these studies has been to estimate both the antenna far-field pattern characteristics (including the gain and polarization) and the near field and terminal characteristics (such as the input impedance), through desirable modeling formulation for microstrip antenna design. Although there are many microstrip antenna arrays that have attractive electrical performance, their realization is based on experiments rather than theoretical evaluation.

A number of papers has presented various approaches to solving the above modeling problem with differing degrees of accuracy and flexibility [1]-[12]. The earliest mathematical model is the transmission-line model. This method assumes

that the fields produced by the electrical surface currents on the conducting patch of the microstrip antenna are equivalent to those produced by a magnetic surface current sheet bounding the patch in the substrate [1,2 and 25]. The merit of this model lies in its simplicity, but it can only treat the rectangular shaped radiator and is not capable of dealing with alternatively shaped radiators.

The more useful and rigorous analytical modeling is the modal-expansion cavity model which considers the microstrip antenna as a thin TM_z-mode cavity with magnetic walls [4]-[5]. The fields between the conducting patch and the ground plane are expanded in terms of a series of cavity resonant modes or eigenfunctions along with their eigenvalues or resonant frequencies associated with each mode. By means of this method, field solutions for both rectangular and circular patch elements with different feed types and locations are much more satisfactorily obtained. However, for other shapes, which have asymmetric and irregular geometry to produce special performance such as a wide bandwidth, the modal-expansion technique is ineffective due to the difficulty in finding the appropriate orthogonal mode vectors.

Numerical analysis techniques are thus more direct and general, when considering arbitrary types of microstrip antennas. The key to analysing microstrip antennas by numerical methods lies in finding either the integral or differential equations which are tenable from the physical point of

view and realizable from the mathematical point of view. The accuracy of the result depends on the computational resources available.

Many numerical techniques have been successfully employed to analyse microstrip antennas. They can be classified into two categories: the finite element method, and the moment method. Carver and Coffey [9] applied the finite element method to deal with the fields interior to a five-sided polygon patch by solving the inhomogeneous wave equation along with an impedance boundary condition (BC) on the patch perimeter walls, i.e.,

$$\frac{\partial^2 u}{\partial x^2} + \frac{\partial^2 u}{\partial y^2} + \frac{\partial^2 u}{\partial z^2} = j\omega J_z \tag{1.1}$$

$$\frac{\partial u}{\partial n} + \alpha u = 0 \qquad \text{B.C. on patch perimeter}$$

where u represents the relative field component. In the variational formulation to solve these equations we have to minimize a functional I(V) [17],

$$I(V) = \iint \left(V_x^2 + V_y^2 - k^2 V^2 + 2j\omega\mu J_z V \right) dA \tag{1.2}$$

$$+ \oint \alpha V^2 \, dl$$

for all permissible functions V(x,y). The particular function V*(x,y) which minimizes the functional is the "best" solution to the problem [9]. By using the area method, which is similiar to the moment method presented in this thesis, the integral of the functional I(V) is reduced to a matrix equation which can be solved by a computer [7]. The area method, with the aid of some numerical processing, produces reasonably accurate results. The moment method, however, seems to be more straightforward and easy to handle in mathematics as well as in numerical computation.

Agrawal and Bailey [3] modeled the microstrip patch as a fine wire grid immersed in a dielectric medium and used the Richmond's reaction integral to evaluate the currents on the wire grid segments. They then modified the results to account for the dielectric slab by a frequency shift and an impedance scaling as obtained from experiment.

Newman and Tulyathan [10] has also dealt with the use of the moment method in treating microstrip antennas. They demonstrated the use of interior surface currents in modeling an air-dielectric microstrip patch. These unknown currents were determined by solving Richmond's reaction formula and the dielectric substrate was taken into account by using the volume equivalence theorem. Carver [9] presents several cautionary notes. First, the surface current J_s, which is found, is that on the interior side of both the patch and the associated ground plane; it is not the surface current

on the exterior side of the patch and cannot be used directly to find the exterior field. Secondly, the method of moments applied to the reaction integral equation does not shed any new light on the mathematical connection between the interior and exterior fields, except insofar as the magnetic surface current M_s on the radiating perimeter walls is formulated correctly.

Recently Bailey and Deshpande proposed a method to analyse the microstrip antenna by Galerkin's method [12]. They first derived the dyadic Green's function which satisfies the boundary conditions for a unit current located in the plane of the microstrip patch. Then, by using Galerkin's method, they solved the integro-differential equation for the unknown patch current. This method avoids the reaction integral, but still calculates only the radiated electromagnetic field inside the dielectric [12].

Pozar presented a moment method solution of input impedance and mutual coupling of microstrip antennas using the same formulation as Newman [10], except that he utilizes rigorous grounded dielectric slab Green's function [24]. Because of this rigorous Green's function, his results were more accurate than those of Newman.

In this thesis, in order to take advantage of the moment method and overcome its disadvantages, new electric and magnetic field integral equations are developed. Initially, the image theory is applied to remove the microstrip ground

plane. The space is then divided into two regions, the dielectric medium and the air space. In both regions the electric and magnetic field vectors are expressed in terms of integral equations involving the tangential field distributions over a closed surface. The continuity of the tangential electric and magnetic field vectors at the interface of the air and dielectric regions is then used to obtain a set of coupled integral equations for the field distributions over the interface plane. By applying the moment method these coupled integral equations are reduced to a matrix equation, the solution of which gives the required field distribution. The computed field distributions are then used to determine the radiated field of the microstrip antenna.

Chapter II briefly discusses the formulation of the integral equations and provides the coupled integral equations for microstrip antennas. In Chapter III, the moment method is described and is applied to the integral equations to derive the matrix equation. The computed results are presented in Chapter IV, which are compared with those of the experimental and approximate methods normally used for analysing microstrip antennas. The effect of microstrip dimensional parameters on its radiation characteristics are also discussed. Finally, Chapter V gives a summary of the results and discusses the main electrical characteristics of microstrip antennas.

Chapter II

THEORY

2.1 INTRODUCTION

The main purpose of this chapter is to present a general theory so that we can deal with most microstrip antenna problems by means of the numerical approach. Theoretically, the difficulty in analysing a microstrip antenna is that the fields propagate in neither homogeneous nor inhomogeneous media. The propagating region is a combination of two homogeneous regions, with a conducting region inserted between these two media. For this reason, we cannot directly apply the moment method to the integral equations to find the current distribution on the conducting patch. We will derive the general form of the electric and magnetic field integral equations in the space-frequency domain and couple the two regions by the boundary conditions to create a set of integral equations which will allow us to determine the unknown surface field distributions. These surface fields will be used as the equivalent sources, by the equivalence theorem, to calculate the antenna characteristics of interest.

2.2 ELECTROMAGNETIC INTEGRAL EQUATIONS

Consider a region with permeability and permittivity of μ and ϵ, respectively. A current I of incremental length dl is located at the origin and directed along the positive z axis, as shown in Fig.2.1. Such a current element Idl can be expressed as

$$\bar{J} = I\, d\ell\, \hat{a}_z \tag{2.1}$$

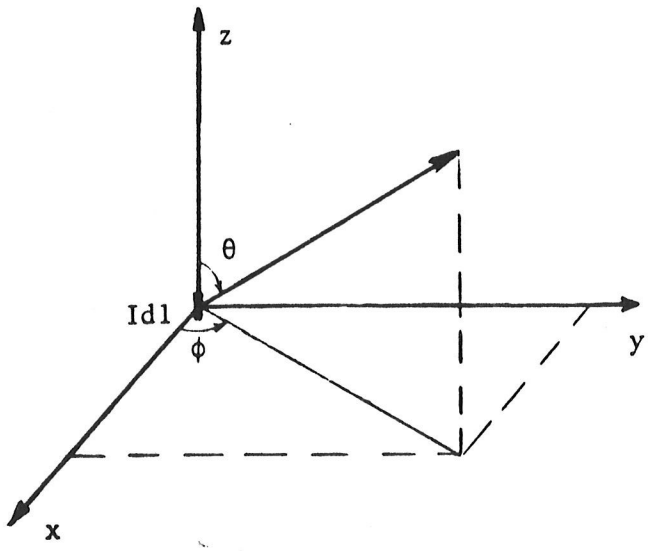

Figure 2.1: A Current Element at the Coordinate Origin

Electromagnetic fields $\bar{E}$ and $\bar{H}$ produced by this current element at an observation point P are [13]

$$d\bar{E}^e = -\frac{j\omega\mu}{4\pi}\left[\bar{J} + \frac{1}{k^2}(\bar{J}\cdot\nabla')\nabla'\right]\Phi\, dv' \tag{2.2}$$

and

$$d\bar{H}^e = \frac{1}{4\pi}\left[\bar{J} \times \nabla'\Phi\right] dv' \tag{2.3}$$

Equations (2.2) and (2.3) can be used to determine the field vectors of a current distribution in the form

$$\bar{E} = -\frac{j\omega\mu}{4\pi}\int\left[J + \frac{1}{k^2}(\bar{J}\cdot\nabla')\nabla'\right]\Phi\, dv' \tag{2.4}$$

and

$$\bar{H}^e = \frac{1}{4\pi}\int \bar{J} \times \nabla'\Phi\, dv' \tag{2.5}$$

Similarly, for a magnetic current source we have

$$d\bar{E}^m = -\bar{M} \times \nabla'\Phi\, dv' \tag{2.6}$$

and

$$d\bar{H}^m = \frac{j\omega\mu}{4\pi}\{-\bar{M} - \frac{1}{k^2}[(\bar{M}\cdot\nabla')\nabla'] dv' \tag{2.7}$$

and

$$\bar{E}^m = \frac{1}{4\pi} \int [-\bar{M} \times \nabla' \Phi \,] \, dv' \tag{2.8}$$

and

$$\bar{H}^m = \frac{j\omega\varepsilon}{4\pi} \int [-\bar{M} - \frac{1}{k^2} (\bar{M} \cdot \nabla') \nabla' \,] \, \Phi \, dv' \tag{2.9}$$

Combining equations (2.4) and (2.8), the total electric field can be computed from the following equation:

$$\bar{E} = \frac{1}{4\pi} \int [-j\omega\mu\bar{J} - \frac{j\omega\mu}{k^2} (\bar{J} \cdot \nabla') \nabla' - \bar{M} \times \nabla'] \, \Phi \, dv' \tag{2.10}$$

Similarly, the total magnetic field can be determined from a combination of equations (2.5) and (2.9). That is

$$\bar{H} = \frac{1}{4\pi} \int [-j\omega\varepsilon \bar{M} - \frac{j\omega\varepsilon}{k^2} (\bar{M} \cdot \nabla') \nabla' + \bar{J} \times \nabla' \,] \, \Phi \, dv' \tag{2.11}$$

When the source distribution is located on a surface, the equivalence principle can be used to replace the currents with the field distributions. Equations (2.10) and (2.11) then take the forms

$$\bar{E} = \frac{1}{4\pi} \int \{-j\omega\mu(\hat{n} \times \bar{H}) - \frac{j\omega\mu}{k^2}[(\hat{n} \times \bar{H})\cdot\nabla'] + (\hat{n} \times \bar{\mathbf{H}}) \times \nabla'\} \Phi \, dS' \qquad (2.12)$$

and

$$\bar{H} = \frac{1}{4\pi} \int \{ j\omega\varepsilon(\hat{n} \times \bar{E}) + \frac{j\omega\varepsilon}{k^2}[(\hat{n} \times \bar{E})\cdot\nabla'] + (\hat{n} \times \bar{H}) \times \nabla'\} \Phi \, dS' \qquad (2.13)$$

When both field and current source distributions are present, the vectors must be determined by including both source types. The equations are general and can be used to investigate any scattering or antenna problem. In the present work, they are used to formulate a set of integral equations suitable for studying microstrip type antennas.

2.3 SURFACE INTEGRAL EQUATIONS AND SINGULARITIES

First of all, it is essential to formulate the surface integral equations for the present problem by applying the equations (2.12) and (2.13). Secondly, the singularity of these surface integral equations must be carefully treated before we perform any computations.

2.3.1 Surface Integral Equations

Although not previously mentioned, one must notice that the differentiability and continuity conditions on $\bar{E}$ (and $\bar{H}$) and the Green's function $\Phi, \nabla\Phi$, and $\nabla^2\Phi$ restrict the applicability of equations (2.12) and (2.13). The observation point $\bar{r}$ and the source point $\bar{r}'$ may not coincide since the singularity at $\bar{r} = \bar{r}'$ would invalidate the equations. In order to circumvent this difficulty, a sphere of radius δ is circumscribed about r as shown in Fig.2.2.

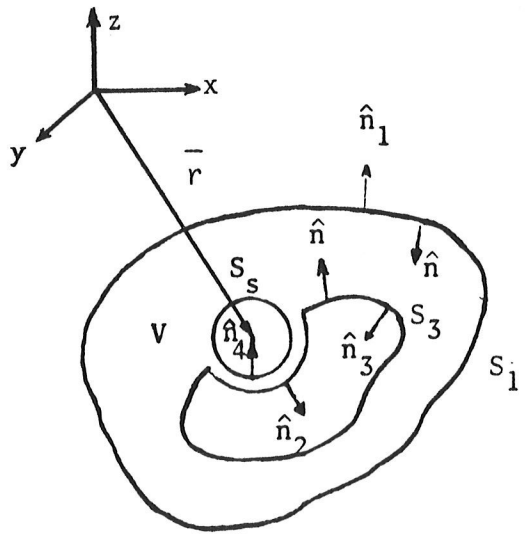

Figure 2.2: The Surfaces in the Derivation of the Integral Equations

The surface integrals are over the surface S, which can be written as the sum of the following surfaces

$$S = S_1 + S_2 + S_3 + S_s \qquad (2.14)$$

The sum of the integrals over S_s and S_2 will be denoted as I and is taken in the limit of vanishing $\delta = |\bar{r}-\bar{r}'|$. With $\delta \to 0$, the phase factors in Φ and $\nabla\Phi$ become negligible. The limiting value of the integrals when r is within S_s can be shown to be [14]:

$$I = - E(r) [4\pi - \Omega_2] \tag{2.15}$$

where Ω_2 is the absolute value of the solid angle subtended by S_2 at r in the limit as δ vanishes. $\Omega_2 = 0$ for r not on the surface and $\Omega_2 = 2\pi$ for r on a smooth portion of ∂V.

Substituting (2.15) into equations (2.12) and (2.13) and considering that the contribution from the integral over S_1 be due entirely from source outside S_1 (This contribution is normally known as the incident field.), we obtain

$$\hat{n} \times \bar{E} = 2\, \hat{n} \times \bar{E}^{inc} + \frac{1}{2\pi} \hat{n} \times \int \{ -j\omega\mu (\hat{n}' \times \bar{H})$$

$$- \frac{j\omega\mu}{k^2} [(\hat{n}' \times \bar{H}) \cdot \nabla'] \nabla' + (\hat{n}' \times \bar{E}) \times \nabla' \} \Phi \, ds' \tag{2.16}$$

Similarly, we obtain the integral equation for the magnetic field

$$\hat{n} \times \bar{H} = 2\, \hat{n} \times \bar{H}^{inc} + \frac{1}{2\pi} \hat{n} \times \int \{ j\omega\varepsilon (\hat{n}' \times \bar{E})$$

$$+\frac{j\omega\varepsilon}{k^2}[(\hat{n}' \times \bar{E})\cdot\nabla']\nabla' + (\hat{n}' \times \bar{H}) \times \nabla'\} \Phi \, ds' \qquad (2.17)$$

Equations (2.16) and (2.17), however, are still not ready for numerical modeling, until we prove the existence of the principal value of their kernels and determine their dependence on the geometry of the self patch (principal area).

2.3.2 Singularities

For the singular integral equations (2.16) and (2.17), the kernels include the scalar Green's function, and its first and second derivatives. The principal value of the kernels which contain Φ and $\nabla\Phi$ have been obtained in many papers. In a recent paper by Yagjian[15], the surface integral is converted to a circular principal value integral using the following formula, derived from a staightforward integration near the singularity of $\bar{r} = \bar{r}'$,

$$\int_{s(r\to s)} \nabla'\Phi \, ds' = \oint_s \nabla'\Phi \, ds' \pm 2\pi\hat{n} \qquad (2.18)$$

Thus, to generalize (2.18) to an arbitrary (regular) principal area, an identity is used,

$$\oint_{s'} \nabla'\Phi \, ds' = \oint_s \nabla'\Phi \, ds' - \int_{\Delta s} \nabla'\Phi \, ds' \qquad (2.19)$$

where the surface integral on the left-hand side of (2.19) excludes the singularity by the arbitrary shaped principal area. The first surface integral on the right-hand side excludes the singularity by a centered circular principal area (denoted by the symbol '0'), and the second integral on the right is an integration over the limiting surface ΔS between the arbitrary and inscribed circular principal areas. The geometry (shape, position, and orientation) of the principal area with respect to the singular point r is specified and maintained as its size shrinks to zero. Because the integral over ΔS does not include the singularity, and because $\Delta s \to 0$ in the limit as the principal area shrinks to zero, this integral can be evaluated with the help of a known integral formula [16]:

$$\int_{\Delta s} \nabla'\Phi \, ds' = \int_{\Delta s} \nabla'_s\Phi \, ds' = \oint_c \frac{\hat{u}_\perp}{R} \, dc - \oint_c \frac{\hat{u}_T}{R} \, dc \qquad (2.20)$$

The second integral on the right-hand side of (2.20) is zero and thus (2.19) and (2.20) substituted into (2.16) yield;

$$\int_{s(r\to s)} \nabla'\Phi \, ds' = \oint_s \nabla'\Phi \, ds' \pm 2\pi\hat{n} + 2\pi\bar{T} \qquad (2.21)$$

where

$$\bar{T} = \frac{1}{2\pi} \oint_c \frac{\hat{u}_T}{R} \, ds \qquad (2.22)$$

As depicted in Fig.2.3, the unit vector $\hat{u}_\perp$ is in the plane of the principal area and perpendicular to its regular boundary C. Thus T is tangent to the surface S, and vanishes for a circular or regular-polygonal principal area centered on the singularity. It is obvious that T is either zero or negligible unless the chosen principal area exhibits significant asymmetry with respect to the singular point.

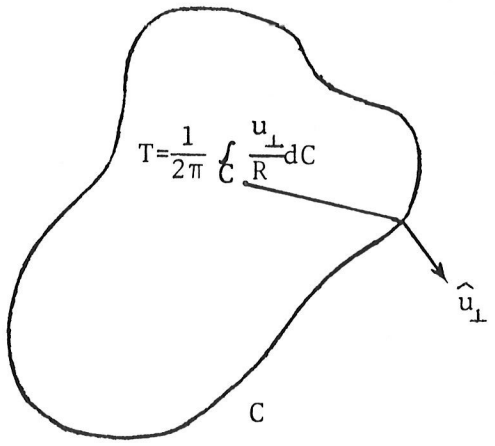

Figure 2.3: The Definition of Tangential Principal Area Vector T

A simpler way for achieving the above objective for the function $\nabla^2\Phi$ is introduced here. As illustrated in Fig.2.4, we consider two circles, A_1 and A_2, centered at the singular point with radii δ_1 and δ_2, respectively. A regular-polygon

is circumscribed to C_1 and inscribed to C_2, where C_1 and C_2 are the perimeters of A_1 and A_2, respectively.

The integration over a symmetric region can be calculated by noting that the operator $\nabla^2\Phi$ in a polar coordinate system is:

$$\nabla^2 = \frac{\partial^2}{\partial r^2} + \frac{2}{r}\frac{\partial}{\partial r} \tag{2.23}$$

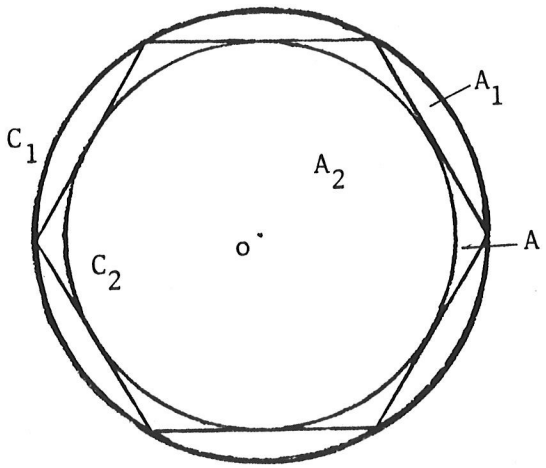

Figure 2.4: The Regular Principal Area for The Singular Point

and after some algebraic manipulation, gives:

$$\nabla^2\Phi = -k^2\frac{1}{r}\,(\cos kr - j \sin kr) \tag{2.24}$$

Thus, The integral over A_1 is given by

$$\int \nabla^2\Phi \, ds = \int_0^{\delta}\int_0^{2\pi} -k^2\,(\cos kr - j \sin kr)\, dr\, d\phi \tag{2.25}$$

As δ_1 approaches zero, the limit of (2.25) becomes

$$\lim_{\delta\to 0} \int_{A_1} \nabla^2\Phi \, ds = \lim_{\delta\to 0} (-k^2\delta) \tag{2.26}$$

Because k is a finite number, the above limit vanishes.

Similarly, for the integral over A_2, one again finds that

$$\lim_{\delta\to 0} \int_{A_2} \nabla^2\Phi \, ds = 0 \tag{2.27}$$

The comparison of equations (2.26) and (2.27) gives

$$\left| \int_{A_2} \nabla^2\Phi \, dS \right| < \left| \int_{A_1} \nabla^2\Phi \, dS \right| \tag{2.28}$$

for $A_2 \in A_1$.

It is apparent that the integral inequalities

$$\left| \int_{A_2} \nabla^2\Phi \, dS \right| \leq \left| \int_{A} \nabla^2\Phi \, dS \right| \leq \left| \int_{A_1} \nabla^2\Phi \, dS \right| \tag{2.29}$$

for $A_2 \in A \in A_1$ is true.

As δ_1 and δ_2 together approach zero, A shrinks to zero. Therefore,

$$\int_{A} \nabla^2\Phi \, ds = 0 \tag{2.30}$$

For an arbitrary shaped principal area, the above proof still holds, as shown in Fig.2.5.

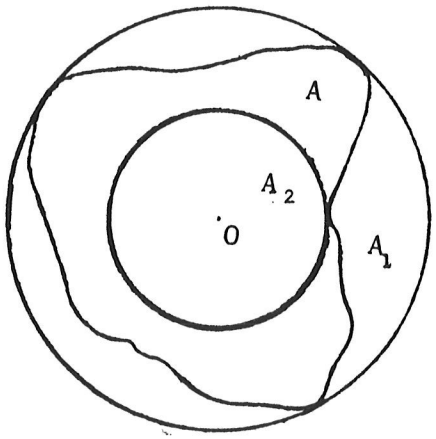

Figure 2.5: The arbitrary Principal Area For the Singular Point

So far, for integral (2.30), we have proven that the principal value exists and an arbitrary principal area can be taken and does not effect the integral itself. As a matter of fact, the kernels of equations (2.16) and (2.17) do not contain $\nabla^2\Phi$, and the proof that is given here is sufficient but necessary, since the partial differential of $\nabla\Phi$ along each direction of any orthogonal coordinate system is equal to or less than the $\nabla^2\Phi$.

For example, in a rectangular coordinate system,

$$\nabla^2\Phi = \frac{\partial^2\Phi}{\partial x^2} + \frac{\partial^2\Phi}{\partial y^2} + \frac{\partial^2\Phi}{\partial z^2}$$

$$= -M\Phi \frac{x^2 + y^2 + z^2}{r} - N\Phi \frac{3}{r} \qquad (2.31)$$

and

$$\hat{i} \cdot \frac{\partial}{\partial x} \nabla\Phi = \hat{i} \cdot [-M\Phi \frac{x}{r} (x\hat{i} + y\hat{j} + z\hat{k}) - N\Phi \frac{1}{r} \hat{i}]$$

$$= - M\Phi \frac{x^2}{r} N\Phi \frac{1}{r} \qquad (2.32)$$

where M and N are the scalar functions of r (see Appendix A).

It is obvious that both of them have almost the same analytic structure, and the function (2.31) is nearly 3 times that of (2.32).

2.4 EQUATIONS FOR MICROSTRIP PATCH ANTENNA

As shown in Fig.2.6, a microstrip antenna consists of a conducting patch (of thickness t) separated from the infinite ground plane by an infinite dielectric slab (of thickness h). A coaxial cable may be used to excite the antenna and induce a field within the dielectric region and over the surface over the substrate.

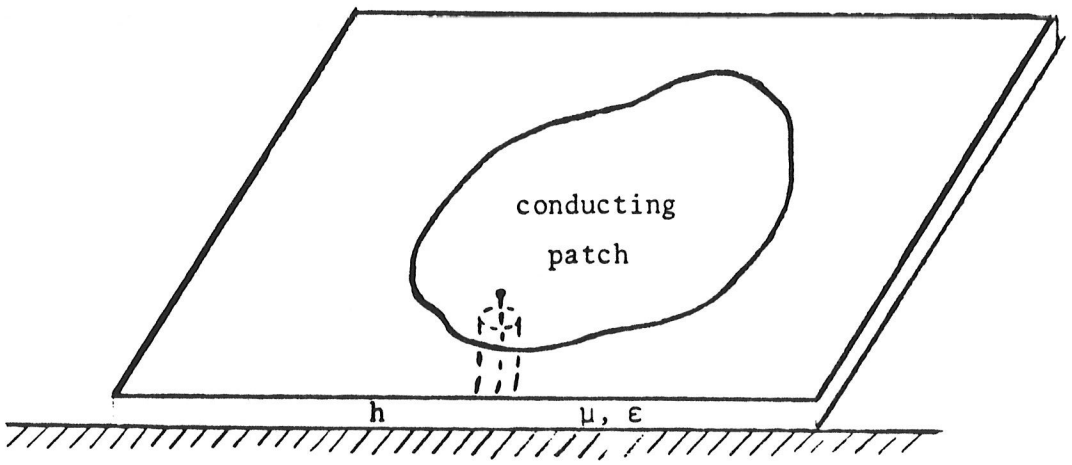

Figure 2.6: The Microstrip Patch Antenna

The radiation field of the antenna is caused by the exciting source, the current induced on the surface of the antenna and the polarization currents within the substrate. However, the latter two current distributions are unknown,

and must be determined. Since, the polarization current is distributed within the dielectric, it involves volume integrals. To restrict the unknowns to a surface distribution, we may divide the region into three parts as shown in Fig.2.7: part I is filled with air, part II is filled with the dielectric of which the permeability and permittivity are μ and ε, respectively, and part III is the perfect conductor. The electromagnetic fields in region II are called interior fields and denoted by $\bar{E}_i$ and $\bar{H}_i$, respectively. The fields in region I are called exterior fields and denoted by $\bar{E}_e$ and $\bar{H}_e$.

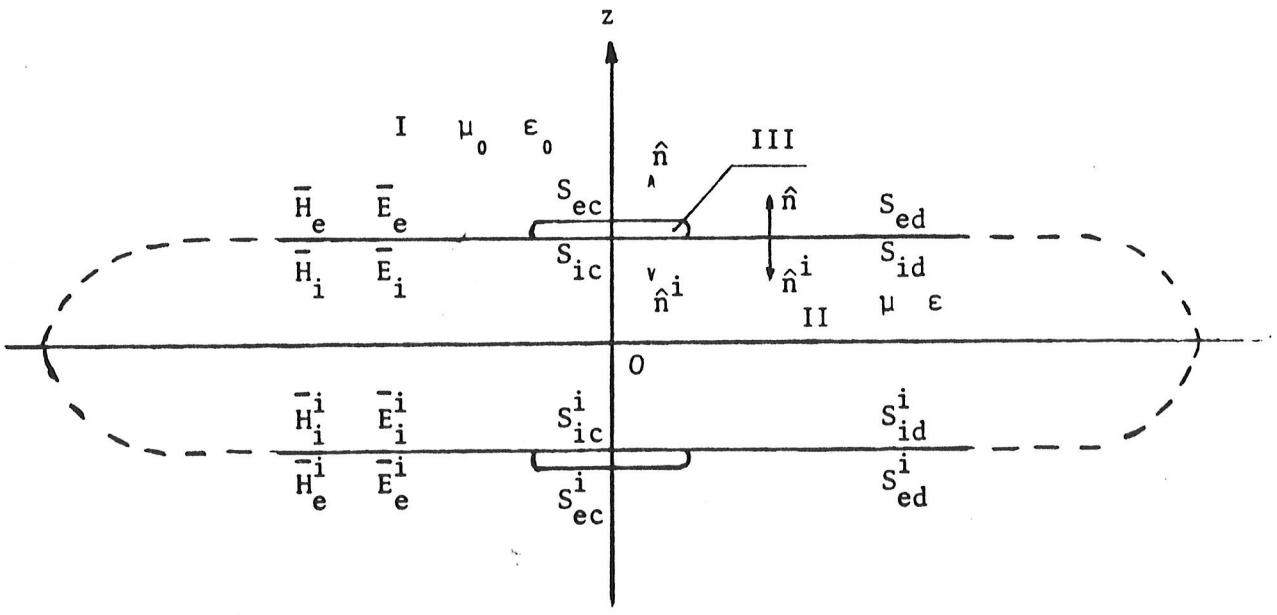

Figure 2.7: The Integral Regions over the Antenna

2.4.1 Interior Fields

Taking a closed surface S_i just inside the intersecting surfaces between region I and II, and between region I and region III, and by applying equations (2.16) and (2.17), a set of surface integral equations are obtained

$$\hat{n} \times \bar{E} = 2\hat{n} \times \bar{E}^{inc} + \frac{1}{2\pi} \hat{n} \times \int_{S_i} \{-j\omega\mu \, (\hat{n}' \times \bar{H})$$

$$- \frac{j\omega\mu}{k^2} [(\hat{n}' \times \bar{H}) \cdot \nabla'] \nabla' + (\hat{n}' \times \bar{E}) \times \nabla' \} \Phi_i ds' \qquad (2.33)$$

and

$$\hat{n} \times H = 2\hat{n} \times \bar{H}^{inc} + \frac{1}{2\pi} \hat{n} \times \int_{S_i} \{ j\omega\varepsilon \, (\hat{n}' \times \bar{E})$$

$$+ \frac{j\omega\varepsilon}{k} [(\hat{n}' \times \bar{E}) \cdot \nabla'] \nabla' + (\hat{n}' \times \bar{H}) \times \nabla' \} \Phi_i ds' \qquad (2.34)$$

where $S_i = S_{id} + S_{ic} + S_{id}^i + S_{ic}^i$, S_{id} is the interface between region I and region II, and S_{ic} is the interface between regions I and III, S_{id}^i and S_{ic}^i are the images of S_{id} and S_{ic}, respectively; and $\hat{n}$ and $\hat{n}'$ are the normal vectors of the surface increments in observation and source points, respectively; $\Phi_i = \exp(jk_i |\bar{r}-\bar{r}'|)/|\bar{r}-\bar{r}'|$.

2.4.2 Exterior Fields

Analogously, taking a closed surface S just outside the interfaces between region II and region I and between regions II and III, by applying equations (2.16) and (2.17), and taking the $\bar{E}^{inc}$ and $\bar{H}^{inc}$ equal to zero, a set of surface integral equations over S is obtained as

$$\hat{n} \times \bar{E} = \frac{1}{2\pi} \hat{n} \times \int \{-j\omega\mu \, (\hat{n}' \times \bar{H}) - \frac{j\omega\mu}{k^2} [(\hat{n}' \times \bar{H})\cdot\nabla'] + (\hat{n}' \times \bar{E}) \times \nabla' \} \Phi_e ds' \qquad (2.35)$$

and

$$\hat{n} \times \bar{H} = \frac{1}{2\pi} \hat{n} \times \int_{S_e} \{ j\omega\varepsilon \, (\hat{n}' \times \bar{E}) + \frac{j\omega\varepsilon}{k^2} [(\hat{n}' \times \bar{E})\cdot\nabla'] + (\hat{n}' \times \bar{H}) \times \nabla' \} \Phi_e ds' \qquad (2.36)$$

where $S_e = S_{ed} + S_{ec} + S^i_{ed} + S^i_{ec}$, S_{ed} is the interface between region II and region I, and S_{ec} is the interface between regions II and III, and S^i_{ed} and S^i_{ec} are the images of S_{ed} and S_{ec}, respectively; and $\Phi_e = \exp(jk_0 |\bar{r}-\bar{r}'|)/|\bar{r}-\bar{r}'|$.

2.4.3 Coupled Integral Equations

The boundary conditions are as follows:

$$\hat{n}_i \times \bar{E}_i = 0$$
$$\hat{n}_e \times \bar{E}_e = 0 \qquad (2.37)$$

at the interfaces between patch and media, and

$$\hat{n}_e \times \bar{H}_e = \hat{n}_i \times \bar{H}_i$$
$$\hat{n}_e \times \bar{E}_e = \hat{n}_i \times \bar{E}_i \qquad (2.38)$$

at the interfaces between the air and substrate. Here the subscripts i and e represent the interior and exterior, respectively; and the superscript i represents the images. As shown in Fig.2.7, S_{id} coincides with S_{ed} and S^i_{id} coincides with S^i_{ed}, and their images coincide with each other. Imposing (2.37) and (2.38) onto equations (2.33) - (2.36), a set of coupled integral equations is obtained for the observation points on the interface between the air and dielectric substrate

$$0 = 2\hat{n} \times \bar{E}^{inc} + \frac{1}{2\pi} \hat{n} \times \int_{S_i} \{-j\omega\mu \, (\hat{n}' \times \bar{H}) - \frac{j\omega\mu}{k^2} [(\hat{n}' \times \bar{H}) \cdot \nabla'] \nabla'$$

$$+ (\hat{n}' \times \bar{E}) \times \nabla' \} \Phi_i ds' + \frac{1}{2\pi} \hat{n} \times \int_{S_e} \{-j\omega\mu \, (\hat{n}' \times \bar{H})$$

$$- \frac{j\omega\mu}{k^2} [(\hat{n}' \times \bar{H})\cdot\nabla'] \nabla' + (\hat{n}' \times \bar{E}) \times \nabla' \} \Phi_e ds' \qquad (2.39)$$

and

$$\hat{n} \times \bar{H}_e + \hat{n} \times \bar{H}_i = 2\hat{n} \times \bar{H}^{inc} + \frac{1}{2\pi} \int_{S_i} \{ j\omega\epsilon (\hat{n}' \times \bar{E})$$

$$+ \frac{j\omega\epsilon}{k^2} [(\hat{n}' \times \bar{E})\cdot\nabla'] \nabla' + (\hat{n}' \times \bar{H}) \times \nabla' \} \Phi_i ds'$$

$$+ \frac{1}{2\pi} \hat{n} \times \int_{S_e} \{ j\omega\epsilon_0 (\hat{n}' \times \bar{E}) + \frac{j\omega\epsilon_0}{k^2} [(\hat{n}' \times \bar{E})\cdot\nabla'] \nabla'$$

$$+ (\hat{n}' \times \bar{H}) \times \nabla' \} \Phi_e ds' \qquad (2.40)$$

Again, imposing (2.37) and (2.38) onto equations (2.33-36), four independent integral equations are obtained. For the observation points on S_{ec}, the interface between the air and conducting patch

$$\hat{n}_e \times \bar{E}_e = \frac{1}{2\pi} \hat{n}_e \times \int_{S_e} \{ -j\omega\mu_0 (\hat{n}_e' \times \bar{H}_e) - \frac{J\omega\mu_0}{k_0^2} [(\hat{n}_e' \times \bar{H}_e)\cdot\nabla']\nabla'$$

$$+ (\hat{n}_e' \times \bar{E}_e) \times \nabla' \} \Phi_e \, ds \qquad (2.41)$$

and

$$\hat{n}_e \times \bar{H}_e = \frac{1}{2\pi} \hat{n}_e \times \int_{S_e} \{j\omega\varepsilon_0 (\hat{n}_e' \times \bar{E}_e) + \frac{j\omega\varepsilon_0}{k_0^2} [(\hat{n}_e' \times \bar{E}_e)\cdot\nabla']\nabla'$$

$$+ (\hat{n}_e' \times \bar{H}_e) \times \nabla'\} \Phi_e ds \qquad (2.42)$$

and for the observation points on S_{ic}, the interface between the dielectric and patch:

$$\hat{n}_i \times \bar{E}_i = 2\hat{n}_i \times \bar{E}^{inc} + \frac{1}{2\pi} \hat{n}_i \times \int_{S_i} \{-j\omega\mu(\hat{n}_i \times \bar{H}_i)$$

$$- \frac{j\omega\mu}{k^2} [(\hat{n}_i \times \bar{H}_i)\cdot\nabla']\nabla' + (\hat{n}_i \times \bar{E}_i) \times \nabla'\} \Phi_i \, ds \qquad (2.43)$$

and

$$\hat{n}_i \times \bar{H} = 2\hat{n}_i \times \bar{H}_i^{inc} + \frac{1}{2\pi} \hat{n}_i \times \int_{S_i} \{j\omega\varepsilon (\hat{n}_i' \times \bar{E}_i)$$

$$+ \frac{j\omega\mu}{k^2} [(\hat{n}_i' \times \bar{E}_i)\cdot\nabla']\nabla' + (\hat{n}_i \times \bar{H}_i) \times \nabla'\} \Phi_i \, ds \qquad (2.44)$$

Equations (2.39), (2.41) and (2.43) are integral equations of the first kind which have two unknowns, while equations (2.40), (2.42) and (2.44) are integral equations of the second kind and have the same unknowns as the former.

Mathematically, the desired electromagnetic fields, the exterior and interior field distributions on the entire interface, can be obtained by solving (2.39) and (2.40) together with any two equations chosen among (2.41) - (2.44) which must contain both interior and exterior unknown fields on both sides of the conducting patch. But in the numerical approach, one has to carefully select the best combination for any given problem [22].

Two comments have to be made here. First, the present equations avoid the differentials of the unknowns. Thus, in numerical modeling, unknowns can be expanded by any kind of basic functions, in particular pulse functions. Second, the equations do not involve the Kottler's boundary line charge integral. Thus they are suitable for open surfaces such as very thin microstrip patch antennas.

Chapter III

NUMERICAL MODELING

3.1 INTRODUCTION

Many techniques, either analytical or numerical, are available for solving integral equations. Of these, the numerical methods make full use of the digital computer capabilities, and enable one to obtain enough accurate numerical results for those problems which are too complex to solve by analytical methods.

As mentioned in Chapter I, the finite element method and moment method have been successfully used for solving the differential and integral systems. In this thesis, the moment method is chosen to solve the set of simultaneous surface integral equations due to its clear physical concept and easily understandable mathematical description. In general, there are two important tasks to complete: the first is to choose the type of base and testing functions to be used, and the second is to model the geometry by a proper segmentation.

For simplificity, the pulse function is selected for both the base and test functions, so that a Galerkin's method could be adapted to our problem. For the present antenna problem, a patch segmentation approach seems to be reasonable.

A central cable fed square microstrip patch antenna is to be modeled as an example. From this example, the different shape patch modeling will follow.

3.2 THE GENERAL METHOD

The moment method described in this section follows Harrington [18].

Equations (2.39) and (2.40) are of the inhomogeneous type with source terms $\bar{E}^{inc}$ and $\bar{H}^{inc}$ respectively. For convenience, they are written in the general form

$$L(f) = g \tag{3.1}$$

where L is the operator in the integral, g is the source, represented by $\bar{E}^{inc}$ or $\bar{H}^{inc}$, and f is the electromagnetic field E or H, the unknown function to be determined.

Let f be expanded in a series of functions f_n, $(n=1,2,\cdots,N)$ in the space - frequency domain, as

$$f = \sum_n \alpha_n f_n \tag{3.2}$$

substituting (3.2) into (3.1), we have

$$\sum_n \alpha_n L(f_n) = g \tag{3.3}$$

We now define a set of testing functions w_m $(m=1,2,\cdots,N)$ in the range of L, and take the inner product of (3.3) with each w_m. The result is

$$\sum_n \alpha_n \langle w_m, L f_n \rangle = \langle w_m, g \rangle \tag{3.4}$$

This set of equations can be written in matrix form as

$$[\, l_{mn}][\, \alpha_n] = [\, g_m] \tag{3.5}$$

where

$$[\, l_{mn}\,] = \begin{bmatrix} < w_1, L f_1 > & < w_1, L f_2 > & \cdots \\ < w_2, L f_1 > & < w_2, L f_2 > & \cdots \\ \cdots & \cdots & \cdots \end{bmatrix} \tag{3.6}$$

and

$$[\, \alpha_n\,] = \begin{bmatrix} \alpha_1 \\ \alpha_2 \\ \cdot \\ \cdot \\ \cdot \end{bmatrix} \tag{3.7}$$

If the matrix [l] is nonsingular, its inverse $[l]^{-1}$ exists.

This solution might be exact or approximate, depending on the choice of f_n and w_m. According to experience, choosing $f_n = w_m$, i.e., using the Galerkin method, the results are satisfactory for engineering purposes and suitable for our problem.

From the mathematical point of view, f_n and w_m should be linearly independent and orthonormal, i.e.,

$$< f_n, f_m > = \delta_{nm} \tag{3.8}$$

and

$$< w_m, w_n > = \delta_{nm} \tag{3.9}$$

For our patch geometry we choose pulse function such that

$$f_n = w_m = \begin{cases} 1, & \text{on } \Delta S_n \\ 0 & \text{otherwise.} \end{cases} \tag{3.10}$$

3.3 APPLICATION OF THE METHOD

A centrally fed square patch microstrip antenna is modeled and serves as an example of how the method is applied. Then, other geometries with the feed point at different locations, may be dealt with in a similar way.

3.3.1 Centrally Fed Square Patch

The geometry and coordinate system used for the modeling is illustrated in Fig.3.1. Assume that the ground plane and dielectric substrate are infinite in extent. The thickness, t, of the perfect conducting patch is much less than the substrate thickness, h, which in turn is much less than the wavelength λ. Using image theory the ground plane is removed and the image of the patch and the substrate, along with the feed probe, are inserted as shown in Fig.3.2.

For this square patch, a rectangular coordinate system is adapted to manipulate equations (2.39) and (2.40) and any two of (2.41-2.44). Since the electromagnetic fields $\bar{E}$ and

$\bar{H}$ are vectors, there are four sets of scalar unknowns in each region that need to be determined.

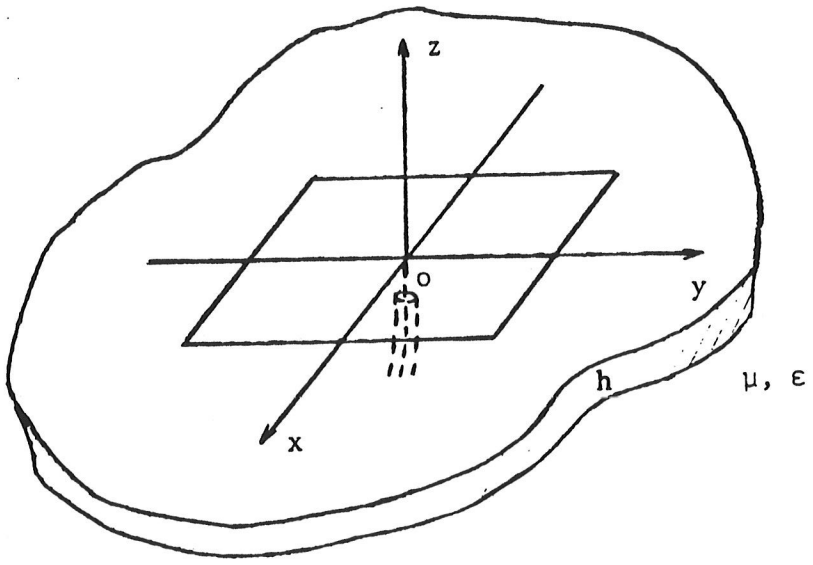

Figure 3.1: The Centrally Fed Patch

In the rectangular coordinate system, as shown in Fig.3.2, they are:

H_{ex}, H_{ey}, H_{ix}, H_{iy}	on the conducting patch
H^i_{ex}, H^i_{ey}, H^i_{ix}, H^i_{iy}	on the image of the conducting patch
H_{ex}, H_{ey}, E_{ex}, E_{ey}	on the interface between S_{id} and S_{ed};
H^i_{ex}, H^i_{ey}, E^i_{ex}, E^i_{ey}	on the interface between S^i_{id} and S^i_{ed};

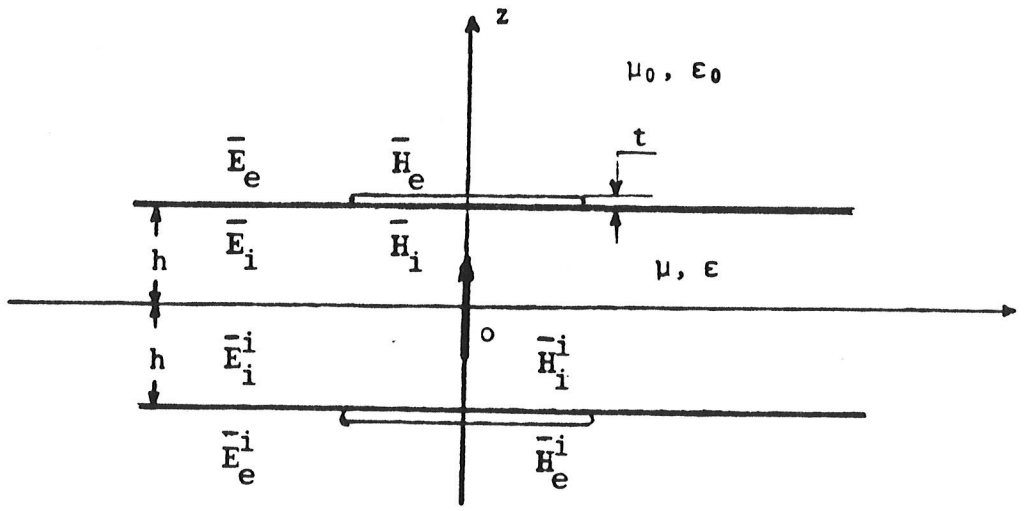

Figure 3.2: The Unknown Fields on the Surface

Expanding equations (2.39), (2.40), (2.42) and (2.44) in the rectangular coordinate system, four independent integral equations are obtained in terms of two transverse directions, x and y. The following are the equations for the observation points on the dielectric surface.

In the x-direction for E

$$0 = 2E_y^{inc} - \frac{1}{2\pi} \int_{S_e} [j\omega\mu\ (\Phi_e - A_e)H_{ex} - j\omega\mu B_e H_{ey}]\ ds'$$

$$- \frac{1}{2\pi} \int_{S_i} [j\omega\mu\ (\Phi_i - A_i)H_{ix} - j\omega\mu B_i H_{iy}]\ ds'$$

$$- \frac{1}{2\pi} \int_{S_{ed}} [\ j\omega\mu\ (\Phi_e - A_e + \Phi_i - A_i)\ H_{ex}$$

$$+ j\omega\mu\ (\ B_e + B_i)\ H_{ey} + (\ D_e + D_i)\ E_{ey}]\ ds' + \int_{S_{ec}^i} \{\ f\ (\ H_{ex}^i,$$

$$H^i_{ey}, H^i_{ix}, H^i_{iy}) \, ds' + \int_{S^i_{ed}} f \, (H^i_{ex} , H^i_{ey} , E^i_{ex} , E^i_{ey}) \, ds' \qquad (3.11)$$

and for H

$$0 = 2H_y^{inc} - \frac{1}{2\pi} \int_{S_{ec}} D_e H_{ey} ds' - \frac{1}{2\pi} \int_{S_{ic}} D_i H_{iy} ds' - \frac{1}{2\pi} \int_{S_{ed}} \{ [j\omega\varepsilon_0 (\Phi_e$$

$$- A_e) + j\omega\varepsilon (\Phi_i - A_i)] E_{ex} + (j\omega\varepsilon_0 B_e + j\omega\varepsilon B_i) E_{ey}$$

$$+ (D_e + D_i) H_{ey} \} ds' + \int_{S^i_{ec}} f \, (H^i_{ey}, H^i_{iy}, H^i_{ex}, H^i_{ix}) \, ds'$$

$$+ \int_{S^i_{ed}} f \, (H^i_{ex}, H^i_{ey}, E^i_{ex}, E^i_{ey}) \, ds' \qquad (3.12)$$

and in the y-direction for E

$$0 = -2E_x^{inc} + \frac{1}{2\pi} \int_{S_{ec}} [j\omega\mu \, B_e H_{ey} - j\omega\mu \, (\Phi_e - C_e) H_{ex}] \, ds'$$

$$+ \frac{1}{2\pi} \int_{S_{ic}} [j\omega\mu \, B_i H_{iy} - j\omega\mu \, (\Phi_i - C_i) H_{ix}] \, ds'$$

$$- \frac{1}{2\pi} \int_{S_{ed}} [j\omega\mu \, (\Phi_e - C_e + \Phi_i - A_i) H_{ey}$$

$$+ j\omega\mu \, (B_e + B_i) H_{ex} + (D_e + D_i) E_{ex}] \, ds' + \int_{S^i_{ec}} f \, (H^i_{ex}, H^i_{ey}, H^i_{ix},$$

$$H^i_{iy}) \, ds' + \int f \, (H^i_{ex}, H^i_{ey}, E^i_{ex}, E^i_{ey}) \, ds' \qquad (3.13)$$

and for H

$$0 = -2H_x^{inc} - \frac{1}{2\pi}\int_{S_{ec}} D_e H_{ex}\,ds' - \frac{1}{2\pi}\int_{S_{ic}} D_i H_{ix}\,ds' + \frac{1}{2\pi}\int_{S_{ed}}\{(D_e + D_i)H_{ex}$$

$$+ [-j\omega\varepsilon_0(\Phi_e - C_e) + j\omega\varepsilon(\Phi_i - C_i)]E_{ey} + (j\omega\varepsilon_0 B_e + j\omega\varepsilon B_i)E_{ex}\}\,ds'$$

$$+ \int_{S_{ec}^i} f(H_{ex}^i, H_{ey}^i, H_{ix}^i, H_{iy}^i)\,ds' + \int_{S_{ed}^i} f(H_{ex}^i, H_{ey}^i, E_{ex}^i, E_{ey}^i)\,ds' \quad (3.14)$$

where A_e, A_i, B_e, B_i, C_e, C_i, D_e, D_i, M_e, M_i, N_e and N_i are scalar functions of $|\bar{r}-\bar{r}'|$ (see Appendix A). To simplify these equations, the integrands involving the image interfaces are denoted by f, since they are same as the integrands in the integrals over their images. One can easily have other four scalar equations for the observation points on both sides of the conductor patch.

As mentioned in Section 2.4.3, we take equations (2.42) and (2.44) combine them with equation (2.39) and (2.40) to constitute a simultaneous set of integral equations to be modeled.

We now divide the patch into M square subsections and use the other size N subsections to cover the interfaces between the air and dielectric medium, as shown in Fig.3.3. Assume that there are N subsections on the whole interface between the air and substrate.

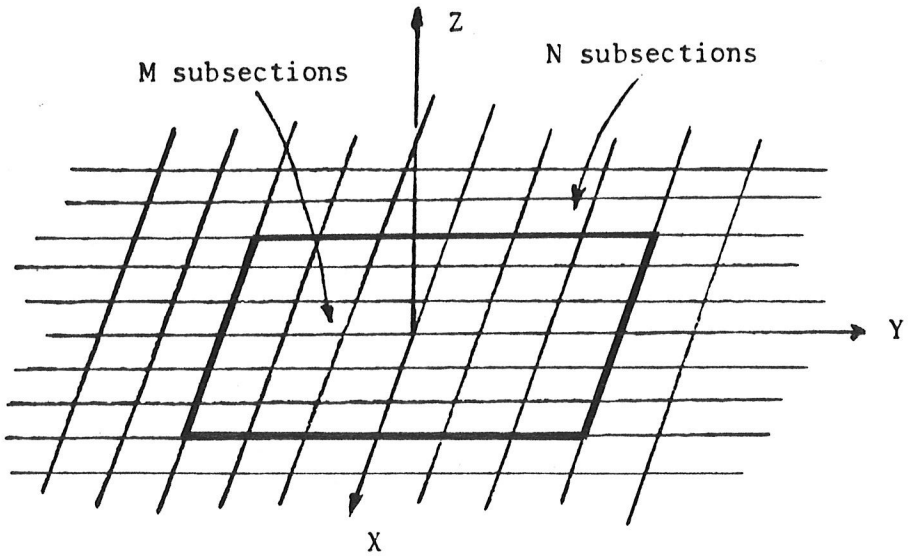

Figure 3.3: The Segmentation of the Whole Antenna

By applying equations (3.3), (3.4) and (3.6) to equations (3.11) - (3.14), we then have the following 4x(N+M)x4 simultaneous equations:

$$\sum_{n}^{M}\sum_{k}^{4} l^{rr}_{mnk\ell}\,\alpha^{r}_{mk} + \sum_{n=M+1}^{M+N}\sum_{k}^{4} l^{rr}_{mnk\ell}\,\alpha^{r}_{mk} + \sum_{n}^{M}\sum_{k}^{4} l^{ri}_{mnk\ell}\,\alpha^{i}_{mk}$$

$$\sum_{n=M+1}^{M+N}\sum_{k}^{4} l^{ri}_{mnk\ell}\,\alpha^{i}_{mk} = g_{n\ell} \qquad (3.15)$$

where $m=1,2,\cdots,M+N$; $\ell=1,2,3,4$. The superscript r denotes the 'real' and i denotes the 'image'. The subscript m rep-

resents the observation point, n represents the field point, k represents the four unknowns and $\ell=1,2,3,4$ corresponding to the independent equations (3.11) - (3.14).

By simple arrangement we can write (3.15) in matrix form as follows

$$[\, l_{st}^{(ri)} \,][\, \alpha_{s}^{(ri)} \,] = [\, g_{t}^{(ri)}] \tag{3.16}$$

where the dimension of $[\, l_{st} \,]$ is 4 X (N+M) X (N+M) X 4 X 4; and $s=t=1,2,\cdots,2x4x(M+N)$.

Using the image and symmetry property, the relationship between the surface electromagnetic fields and their images, as shown in Fig.3.4, are

$$\begin{aligned}
\hat{n}_i \times \bar{H}_i &= -\hat{n}_i^i \times \bar{H}_i^i \\
\hat{n}_i \times \bar{E}_i &= \hat{n}_i^i \times \bar{E}_i^i \\
\hat{n}_e \times \bar{H}_e &= -\hat{n}_e^i \times \bar{H}_e^i \\
\hat{n}_e \times \bar{E}_e &= \hat{n}_e^i \times \bar{E}_e^i
\end{aligned} \tag{3.17}$$

The matrix equation (3.16) can be partitioned as

$$\begin{bmatrix} l^{rr} & l^{ri} \\ l^{ir} & l^{ii} \end{bmatrix} \begin{bmatrix} \alpha^r \\ \alpha^i \end{bmatrix} = \begin{bmatrix} g^r \\ g^i \end{bmatrix} \tag{3.18}$$

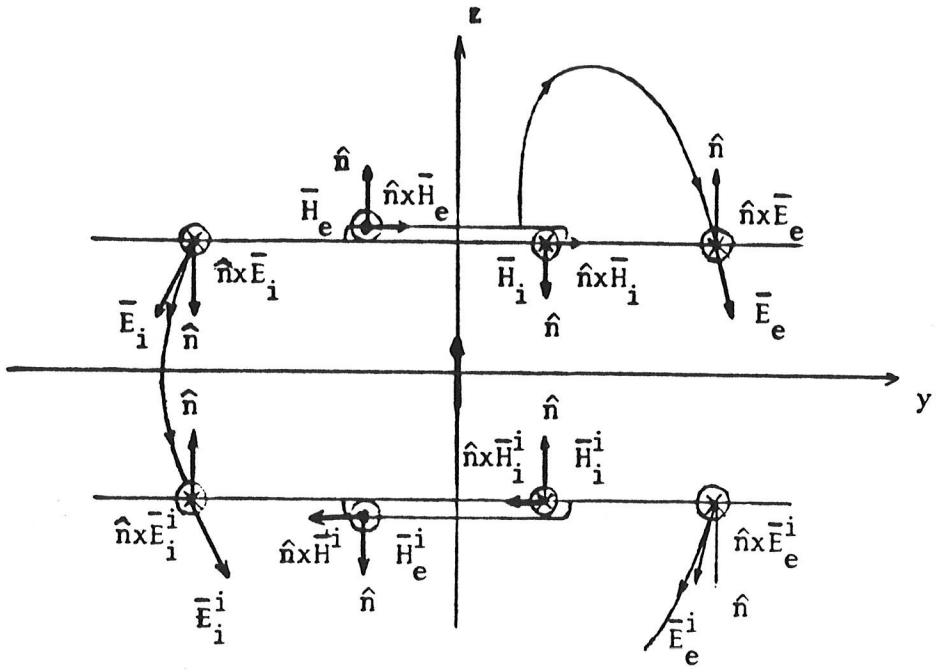

Figure 3.4: The Relationship of the Real and Image Field Vector

Considering the symmetry of the structure as illustrated in Fig.3.4, and that the normal vectors n and n' are opposite to each other, one arrives at

$$\begin{aligned} \alpha^r &= -\alpha^i \\ g^r &= g^i \\ \alpha^r &= \alpha^i \\ g^r &= g^i \end{aligned} \qquad (3.19)$$

From (3.18), we get

$$l^{rr}\,\alpha^{r} + l^{ri}\,\alpha^{i} = g^{r}$$
$$l^{ir}\,\alpha^{r} + l^{ii}\,\alpha^{i} = g^{i} \qquad (3.20)$$

Applying (3.17) and (3.19) to (3.20), we have

$$(l^{rr} - l^{ri})\,\alpha^{r} = g^{r}$$
$$(l^{rr} + l^{ri})\,\alpha^{r} = g^{r} \qquad (3.21)$$

Taking $l = l^{rr} - l^{ri}$ for the magnetic fields and $l = l^{rr} + l^{ri}$ for the electric fields and $\alpha = \alpha^{r}$, a simplified matrix is obtained in the form

$$[\,l_{st}\,][\,\alpha_{s}\,] = [\,g_{t}\,] \qquad (3.22)$$

The dimension of the matrix $[\,l_{st}\,]$ is reduced to (N+M) X 4 X 4, with matrix entries of

$\alpha_s = H_{ex}$
$\alpha_s = H_{ey}$ unknowns on conducting
$\alpha_s = H_{ix}$ patches
$\alpha_s = H_{iy}$
$\alpha_s = H_{ex}$
$\alpha_s = H_{ey}$ unknowns on the dielectric
$\alpha_s = E_{ex}$ intersurface
$\alpha_s = E_{ey}$.

The entries of the coefficient matrix are obtained from equations (3.11) -(3.14) (see Appendix B).

3.3.2 The Excitation Source

Usually, a microstrip antenna is excited either by a microstrip line or by a coaxial type feed, corresponding to a voltage or a current source. The antenna investigated here is fed coaxially, although it could just as easily be fed by a microstrip line at an edge. Since h, the thickness of the substrate, is much less than a wavelength, the current flowing along the probe is considered as a single unit. Thus, this feed can be considered as a delta current source located at (0, 0, z) given by

$$\bar{J} = \hat{k}\, J_z(x, y, z)\, \delta(x)\, \delta(y) \tag{3.23}$$

as shown in Fig.3.5.

This current source is contained within the volume of the dielectric substrate. The electromagnetic fields induced by this source can be directly determined by applying equations (2.10) and (2.11). That is, $\bar{E}^{inc}$ and $\bar{H}^{inc}$ in equations (2.39) and (2.40) can be evaluated by substituting (3.23) into (2.10) and (2.11) to obtain

$$\bar{E}^{inc} = \frac{1}{4\pi} \int [\, -j\omega\mu\, \bar{J} - \frac{j\omega\mu}{k^2} (\bar{J}\cdot\nabla')\, \nabla' \,]\, \Phi \, dv' \tag{3.24}$$

and

$$\bar{H}^{inc} = \frac{1}{4\pi} \int [\ \bar{J} \times \nabla' \Phi\ ]\, dv' \tag{3.25}$$

Taking the inner product of (3.24) and (3.25) with w_m as previously described, then the g terms, excitation terms corresponding to the equation (3.15), are given by:

$$\begin{aligned}
g_{n1} &= \frac{j\omega\mu}{k^2} \frac{1}{r} M h^2 (y_n - y_0)\, \Phi \\
g_{n2} &= \frac{-j\omega\mu}{k^2} \frac{1}{r} M h^2 (x_n - x_0)\, \Phi \\
g_{n3} &= \frac{1}{2r} N h (x_n - x_0)\, \Phi \\
g_{n4} &= \frac{1}{2r} N h (y_n - y_0)\, \Phi
\end{aligned} \tag{3.26}$$

where $n=1,2,\cdots,M+N$; $\ell=1,2,3,4$. This can be easily written as a column matrix, $[\ g_t\ ]$. Placing this matrix into (3.22) allows the equation to be solved by common numerical methods.

We have so far completed the numerical modeling of a square patch microstrip antenna fed at its center by a current source. For arbitrary feed of the source location, the whole modeling procedure is the same as above, except that

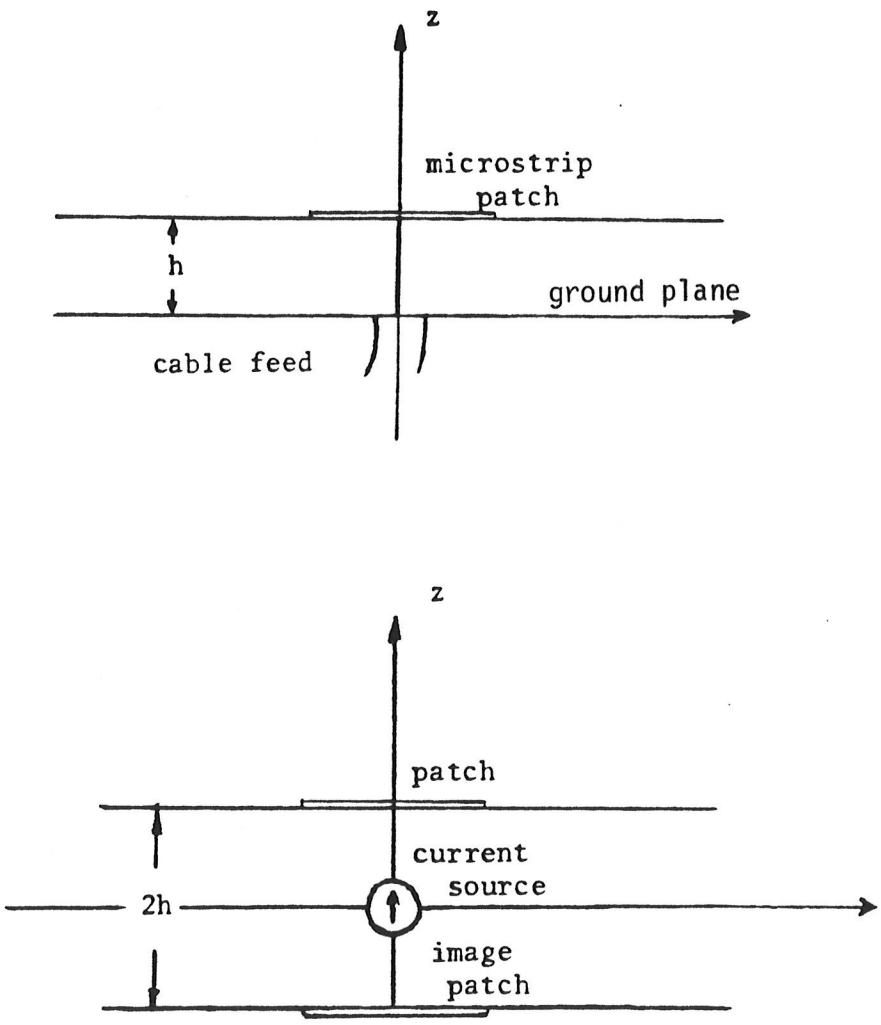

Figure 3.5: The Current Source Excitation

we must change the coordinates of the source location in equation (3.23).

3.4 RADIATION PATTERN AND THE INPUT IMPEDANCE

3.4.1 Radiation Pattern

The main far field characteristic obtained in this section is the radiation pattern. The electric and magnetic fields in the far zone produced by a microstrip antenna are evaluated by substituing electric and magnetic current sources,

$$\bar{J}_S = \hat{n} \times \bar{H}_e \tag{3.27}$$

and

$$\bar{M}_S = \bar{E}_e \times \hat{n} \tag{3.28}$$

into the surface integral equations (2.16) and (2.17), with the E_e and H_e determined by the moment method presented in the previous section.

To determine the scalar Green function, $\Phi = \exp(jk|\bar{r}-\bar{r}'|)/|\bar{r}-\bar{r}'|$, in far zone ($\bar{r} >> \bar{r}'$) we use

$$|\bar{r} - \bar{r}'| \rightarrow r - r' \cos\xi \tag{3.29}$$

as shown in Fig.3.6.

For the conventional coordinate orientation shown in Fig.3.7 we have the transformations

$$x = r \sin\theta \cos\phi$$

$$y = r \sin\theta \sin\phi \qquad (3.30)$$

$$z = r \cos\theta$$

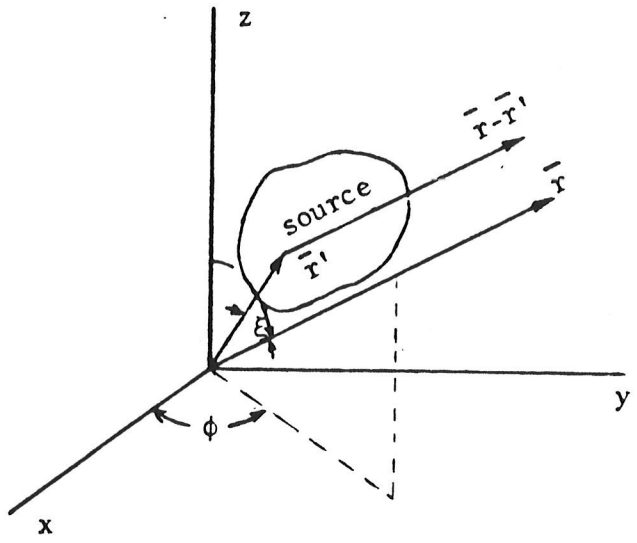

Figure 3.6: Geometry for Evaluating the Radiation Field

To obtain r'cos , we form

$$r\, r' \cos\xi = x\, x' + y\, y' + z\, z' \qquad (3.31)$$

Substituting (3.30) into (3.31), we obtain

$$r' \cos\xi = (x' \cos\phi + y' \sin\phi) \sin\theta + z' \cos\theta \qquad (3.32)$$

Thus, the scalar Green's function in the far zone is

$$\Phi = \frac{e^{-jkr}}{r} e^{jkr'\cos\xi} \tag{3.33}$$

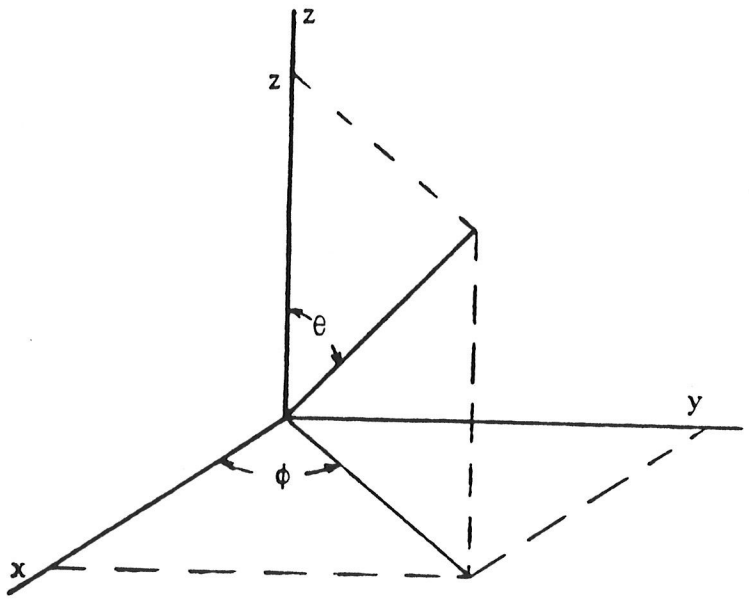

Figure 3.7: Conventional Coordinate Orientation

Using the field equivalence principles, the fields in the far zone can be determined by substituting the electric and magnetic surface currents, (3.27) and (3.28), into equation

(2.16) or (2.17), respectively, and by taking the integral over the entire surface of the antenna, the aperture plane, we get

$$\bar{E} = \frac{1}{4\pi} \int_S \{-j\omega\mu\bar{J} - \frac{j\omega\mu}{k^2}[(\bar{J}\cdot\nabla')] - \bar{M} \times \nabla'\} \Phi \, ds' \qquad (3.34)$$

The far zone field can also be obtained by only substituting the electric surface current over the aperture plane, to give

$$\bar{E} = \frac{1}{4\pi} \int_S [-j\omega\mu\bar{J} - \frac{j\omega\mu}{k^2}(\bar{J}\cdot\nabla')] \Phi \, ds' \qquad (3.35)$$

or, by only using the magnetic surface current over the dielectric interface (the aperture plane excluding the conducting patch), to give

$$\bar{E} = \frac{1}{4\pi} \int_{S-S_c} -\bar{M} \times \nabla'\Phi \, ds' \qquad (3.36)$$

3.4.2 The Input Impedance

The near field characteristics are easy to find using the described technique. Since the field distributions both internal and external to the interface can be correctly deter-

termined, the fields at every point in the interior space can be directly obtained by using the corresponding surface field distributions as the electric and magnetic current sources in equations (2.16) and (2.17). Thus, all near field parameters can be found on this basis. For instance, the very important parameter, the input impedance, can be obtained by the simple equation [20]

$$Z_{in} = - \frac{1}{|I_{in}|^2} \int_0^h E_z(x_o, y_o) I^*(z') dz' \qquad (3.37)$$

and

$$Z_{in} = -h E_z(x_o, y_o) / I_{in} \qquad (3.38)$$

We only need to determine the normal component of the electric field, E , at the feed point, (x_o, y_o).

All the above formulations can be applied to any shape microstrip antenna since no special shape assumption was made during the derivation. One needs to carefully segment the antenna patch and the surrounding dielectric surfaces, and to choose a suitable coordinate system in expanding the electromagnetic field equations for each special geometry. Programming techniques can also be applied to computation procedure in order to save computation resoures.

Chapter IV

RESULTS AND DISCUSSION

The main goal of this thesis is to introduce a new analysis technique for microstrip antennas. With this aim, numerical results, obtained by applying the electric-field integral and magnetic-field equations developed in Chapter II and III to the square patch antennas, are presented in this chapter. First of all, considerable attention is paid to finding the electromagnetic field distribution on the outside of the microstrip antenna, including the dielectric substrate region, since the characteristics of both near and far fields are based upon this field distribution . By utilizing the equivalence principle for integral equations (2.12) and (2.13), the radiation patterns are then obtained. Effort has been put into analysing the patterns to determine how the radiation fields are affected by the surface currents and other factors. The effect of different combinations of equations (2.41-2.44) is also presented in this chapter.

Measurement and numerical results, including those calculated by other approximate methods, are included for the square and rectangular patch microstrip antennas with dimensions $\lambda_g/4$ and $\lambda_g/2$ for both a center-feeding and side-feed

excitation. All the antennas were made of copper-clad 1/16 inch thick substrate of relative permittivity 2.32. In the numerical analysis, the losses in the conductor and the dielectric material are ignored and the patch conductivity is assumed to be infinite. Some typical results, comparison and explanation are given in this chapter. The geometries of these antennas were shown in Fig.4.1.

A series of computing programs was written in FORTRAN language by the author. All computations presented in this chapter were performed on the AMDAHL 470/V8 system installed at the COMPUTER CENTER of University of Manitoba.

The empirical data is obtained with an automated digital antenna measurement system in the electromagnetic anechoic chamber at the Antenna Laboratory of the Department of Electrical Engineering.

4.1 FIELD DISTRIBUTION

The moment method developed in this thesis computes both electric current on the conducting patch and the tangential field distributions on the dielectric substrate. The matrix size therefore depends not only on the patch size but also on the extent of field distributions on the dielectric. It is expected that the latter distribution should depend on the antenna physical parameters. In this section, we intend to investigate this relationship.

Fig.4.1 illustrates the geometry and segmentation of a half wavelength square patch antenna. The operating frequency is 2.0 GHz. Figs 4.2-5 show the computed tangential components of the electric and magnetic fields of this antenna along x = 0.2542 λ_g, y = 0.2542 and 0.00417 λ_g, respectively. The antenna patch is a perfect conductor and the dielectric slab has a thickness of 0.1585 cm and its relative permittivity is 2.32. In all computations the combination of the magnetic - field integral equations, (2.42) and (2.44), for the field points on both sides of the patch are used.

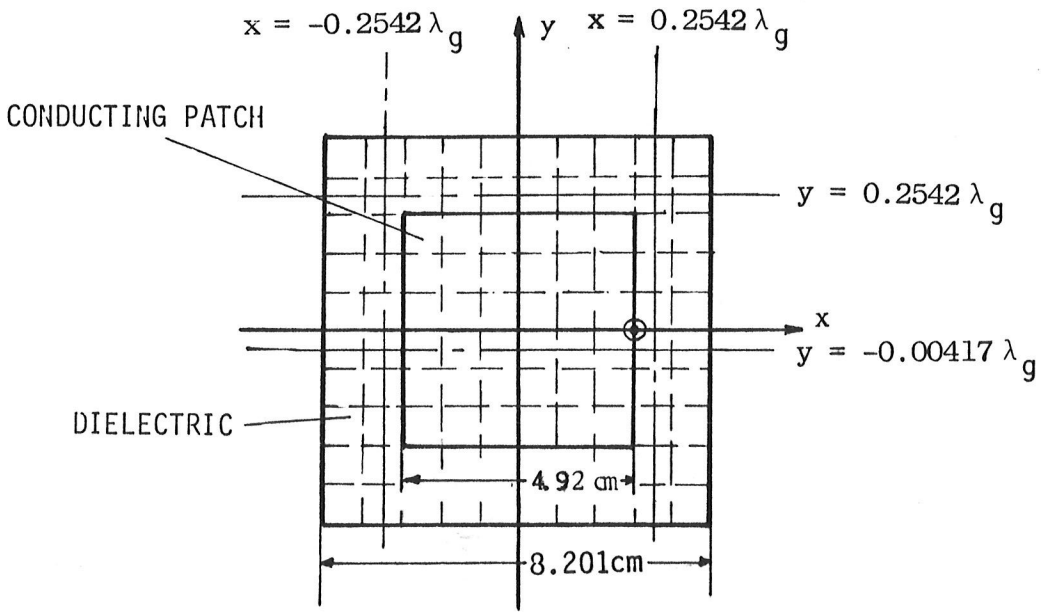

Figure 4.1: Geometry and Segmentation for Field Distributions

λ = 14.896 cm

λ_g = 9.841 cm

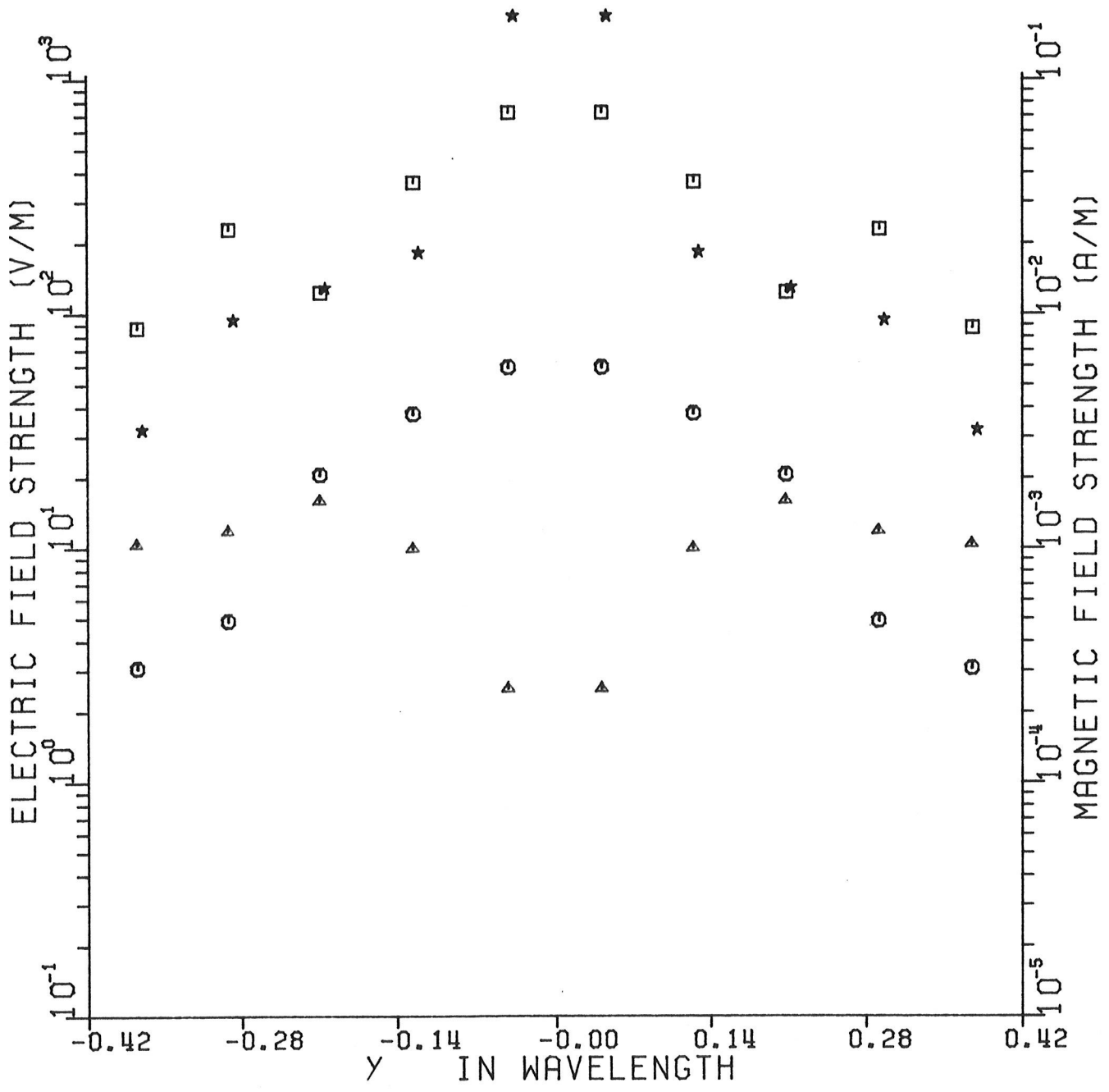

FIGURE 4. 2: FIELD DISTRIBUTIONS ALONG X = 0.2542 λ_g

⊡	H_x
★	H_y
⊙	E_x
△	E_y

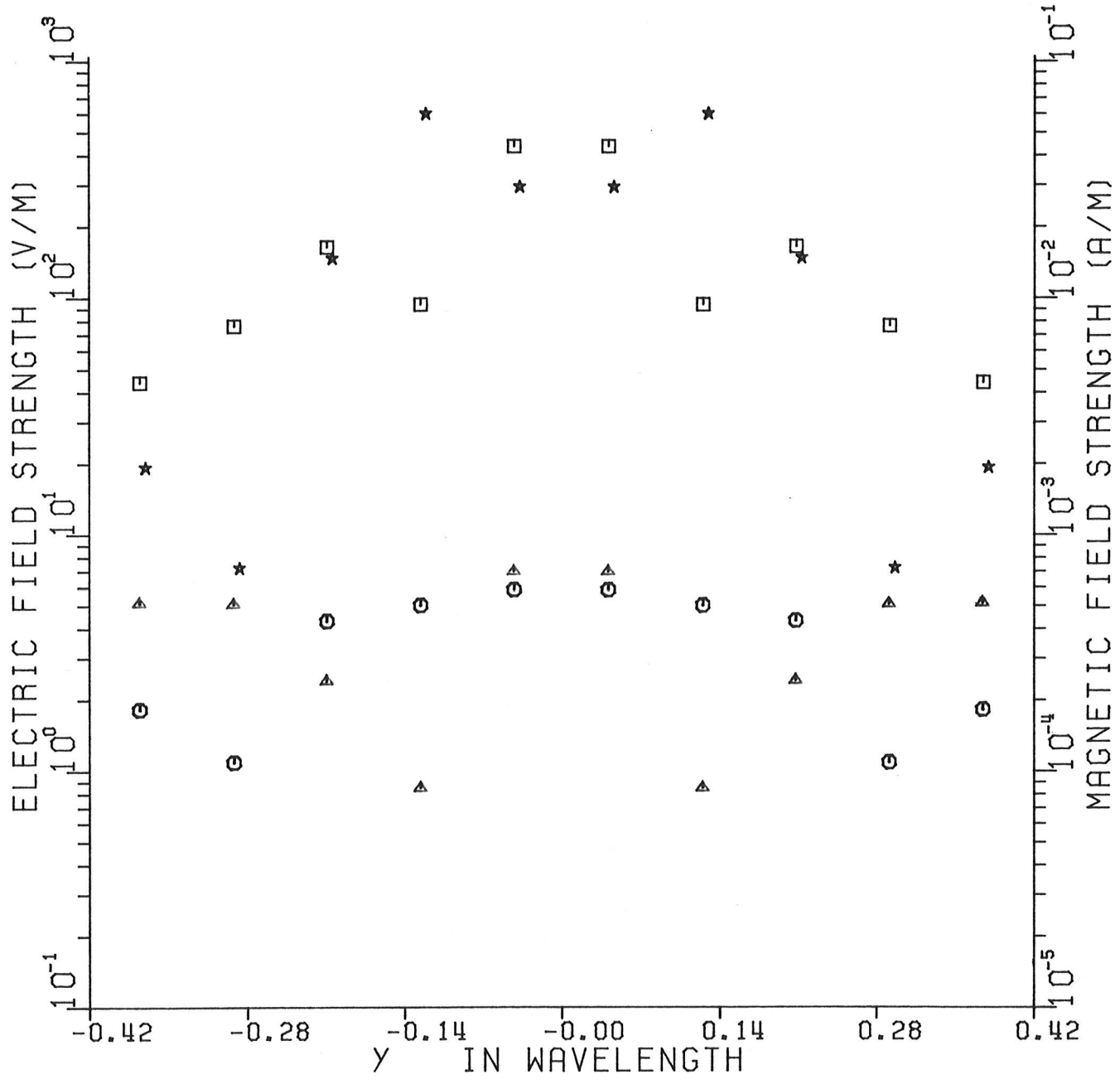

FIGURE 4. 3: FIELD DISTRIBUTIONS ALONG X = -0.2542 λ_g

□	H_x
★	H_y
○	E_x
△	E_y

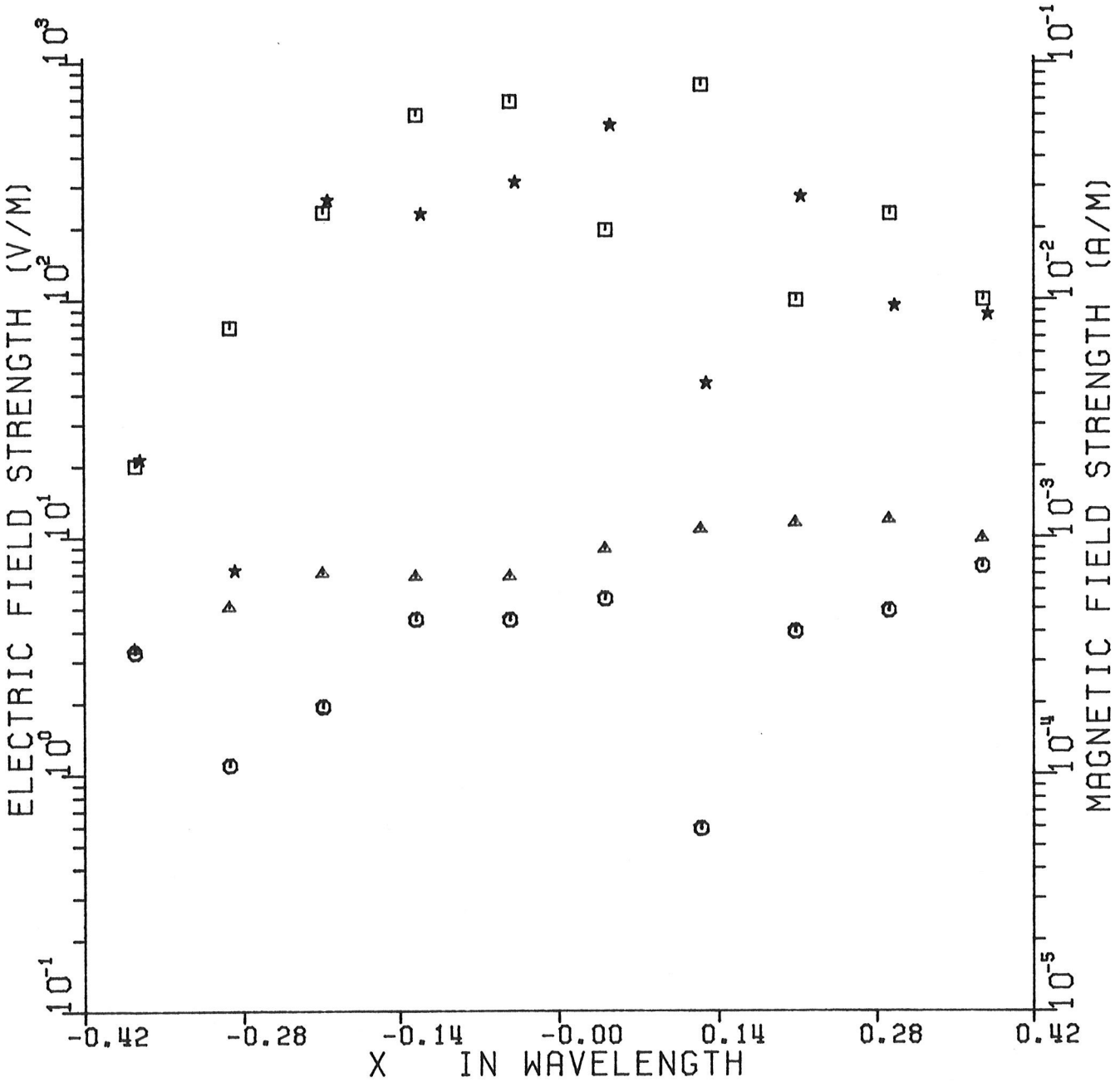

FIGURE 4. 4: FIELD DISTRIBUTIONS ALONG Y = $\pm 0.2542\ \lambda_g$

□	H_x
★	H_y
⊙	E_x
△	E_y

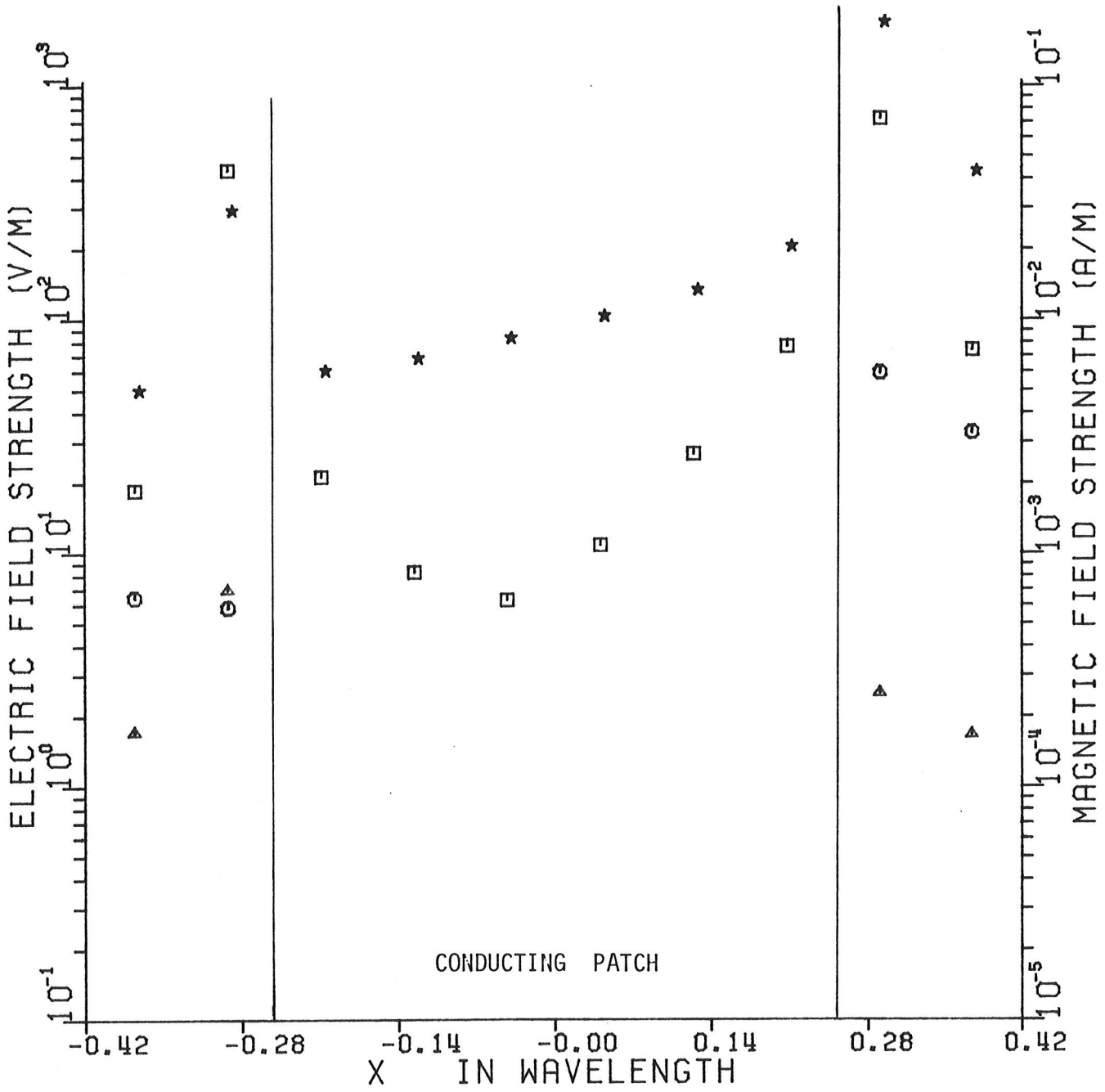

FIGURE 4. 5: FIELD DISTRIBUTIONS ALONG Y = $\pm 0.00417\ \lambda_g$

⊡	H_x
★	H_y
⊙	E_x
▲	E_y

Since the geometry and the excitation point are symmetric about the x - axis, both E_x and H_y are symmetric while E_y and H_x are mirror images with respect to the x - axis. Thus the radiation fields $E_\theta(\theta)$ at $\phi = 0^0$ and 180^0 plane and $E_\phi(\theta)$ at $=90^0$ and 270^0 plane depend only on the surface fields E and H .

Fig.4.2 shows that the distribution of |E | just outside the radiation wall at x= 0.2542 λ_g (the radiation walls locate at $x=\pm 0.25\lambda_g$) exhibits the cosine type variation, i.e., its maximum value is at y=0 ($x= 0.2542\lambda_g$). The same is true for $|H_y|$ and $|E_x|$ in Fig.4.3., but the variation of $|H_y|$ is not exactly the same as that of $|E_x|$.

Fig.4.5 shows the field distribution along the x - axis. Near the edges of the conductor the component of $|H_x|$ is singular and the results indicate that it increases near the conductor edges.

4.2 COMPARISON OF COMPUTED AND MEASURED RADIATION PATTERNS

A comparison between the computed and measured radiation patterns is carried out in this section.

Figs 4.7-10 give the computed and measured radiation patterns of the antenna for the geometry and the segmentations of Fig.4.6. The measured patterns were taken in both the E - and H - planes, corresponding to the computed $E_\theta(\theta)$ and $E_\phi(\theta)$ patterns in the $\phi = 0^0$ and 180^0 and $\phi = 90^0$ and 270^0 planes, respectively. To facilitate the comparison both ex-

perimental and numerical results are presented on the same graph.

The comparison shows that there is very good agreement between computed and measured $E_\phi(\theta)$ patterns. For $E_\theta(\theta)$, their difference increases with frequency. The reason is that the dielectric slab and ground plane are assumed to be infinitly large. However in the numerical solution, the size of both dielectric slab and ground plane are assumed to be about a wavelength. According to our experience, the size of ground plane affects mostly $E_\theta(\theta)$, and not $E_\phi(\theta)$. This is shown in Appendix C. As shown in Fig.C.2, for an air filled disk, the radiation fields $E_\phi(\theta)$ in the upper half plane are exactly same for two different sizes of the ground plane, on the other hand Fig.C.3 shows the strong dependence of $E_\theta(\theta)$ on the ground plane size. In our case, the dielectric slab reduces this difference to some degree because of its high permeability, which concentrates the fields to the region between the two conducting planes. However, the finite ground plane still affects $E_\theta(\theta)$. This deficiency could be improved by increasing the number of subpatches on the dielectric surface, which in turn demands excessive memory space.

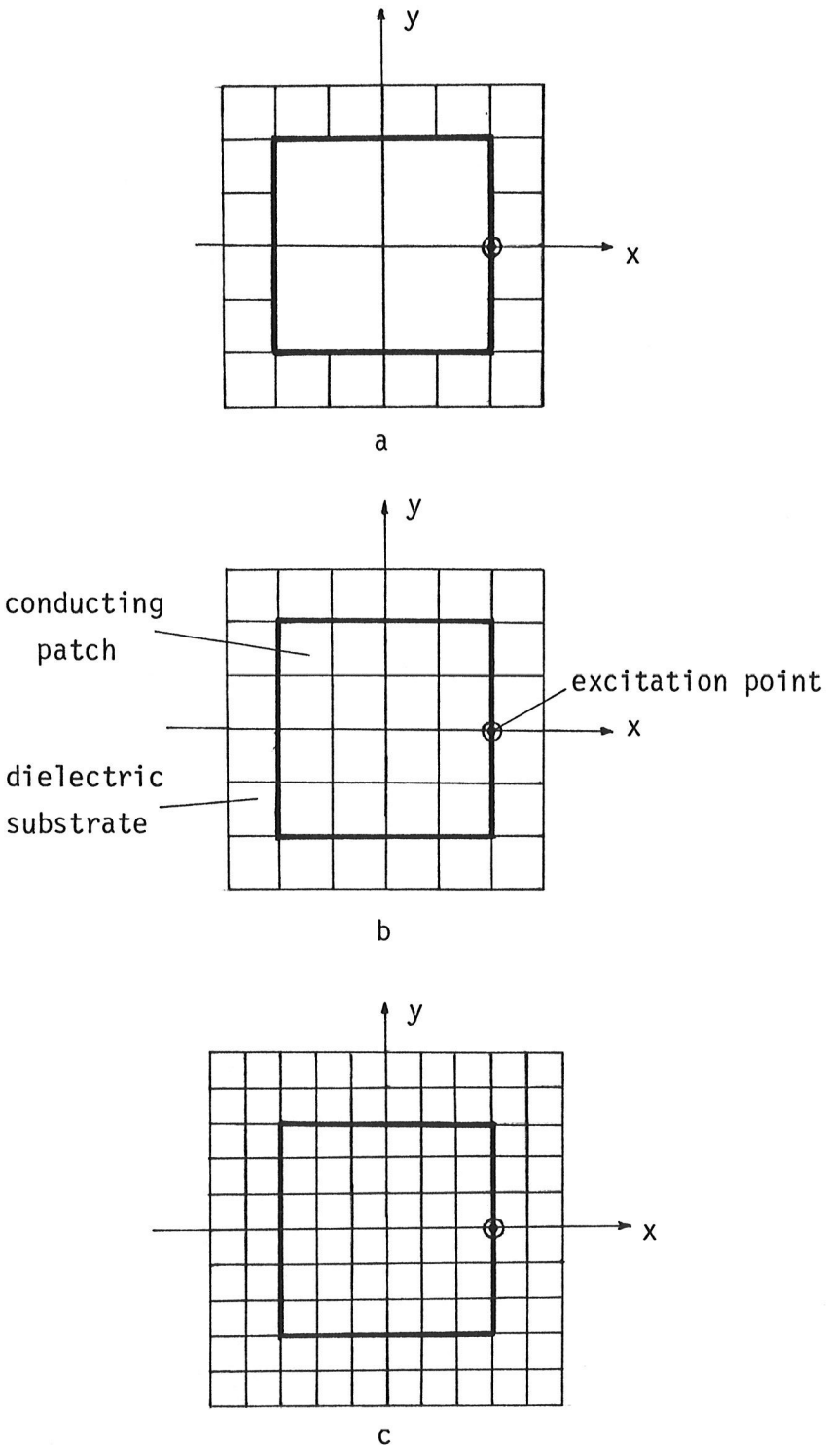

Figure 4.6: Investigated Antenna Segmentations

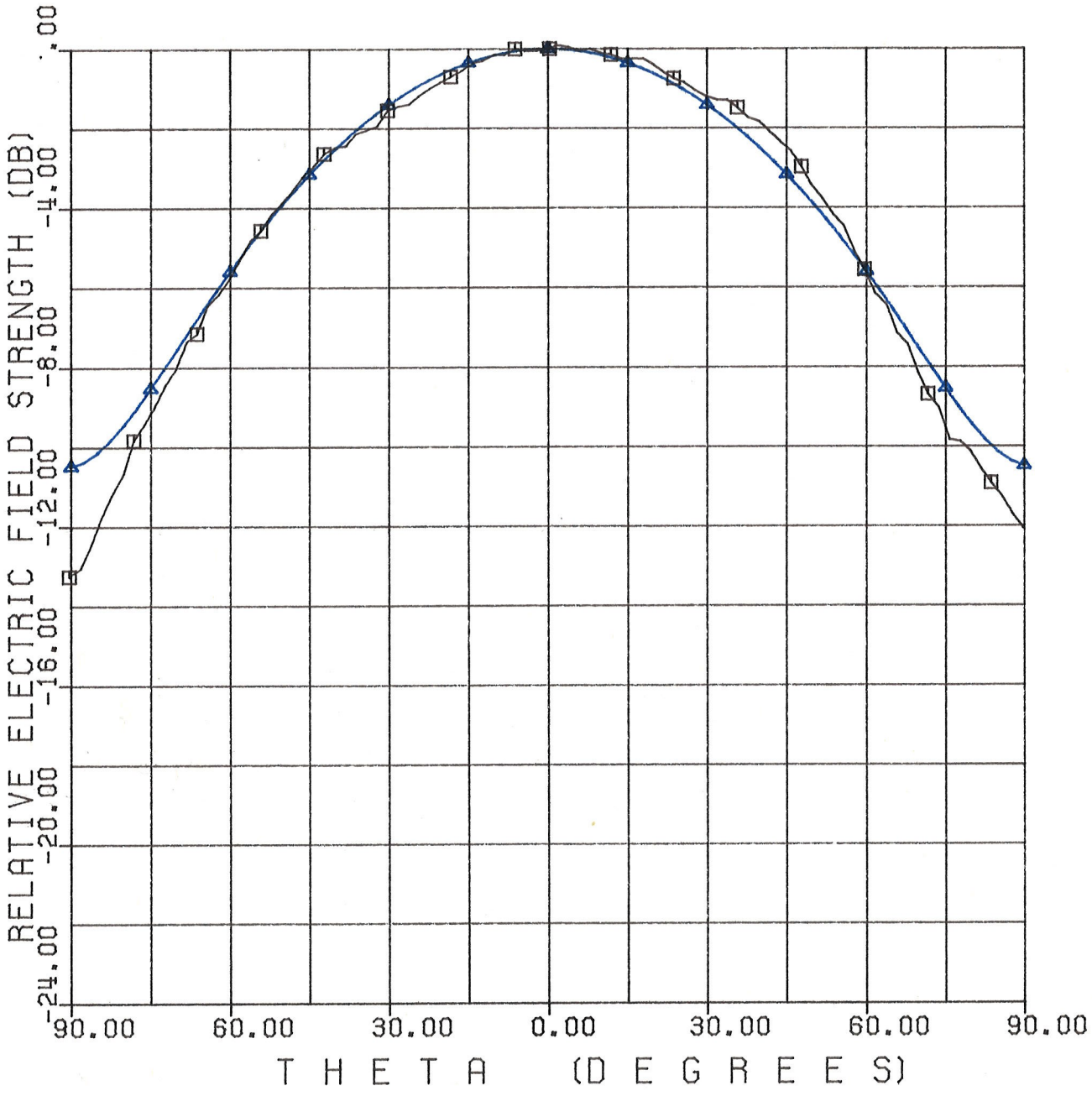

FIGURE 4. 7 COMPARISON OF THE EXPERIMENTAL AND THE NUMERICAL DATA ; $E_{\phi}(\theta)$, FR = 2.0 GHZ , ϕ = 90 ^{0} AND 270 ^{0}

□ EXPERIMENTAL

△ NUMERICAL; SEGMENTATION BASED ON FIG.4.6 (b)

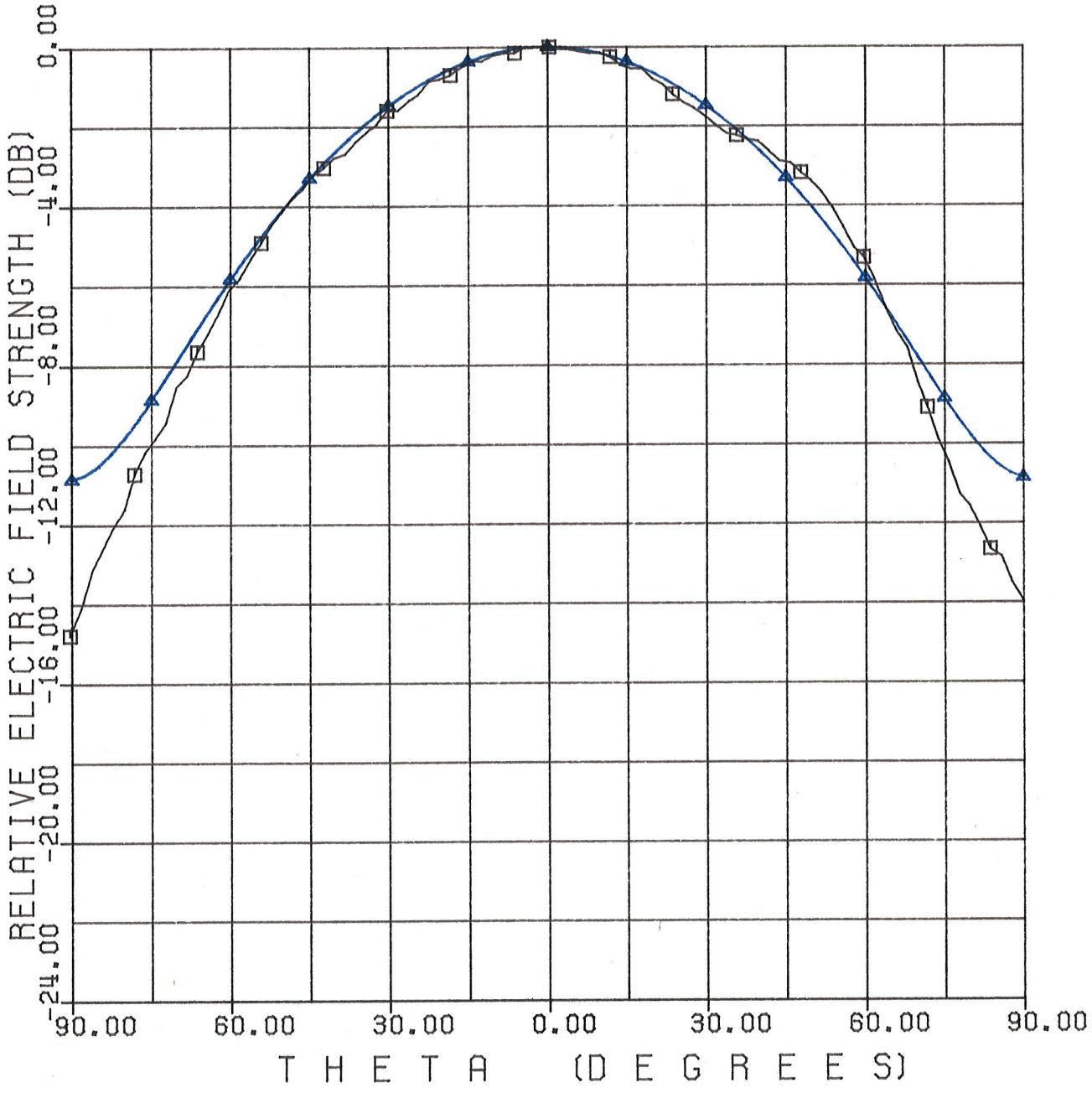

FIGURE 4. 8: COMPARISON OF THE EXPERIMENTAL AND THE NUMERICAL DATA ; $E_{\phi}(\theta)$, FR = 2.1 GHZ , ϕ = 90^{0} AND 270^{0}

□ EXPERIMENTAL

△ NUMERICAL; SEGMENTATION BASED ON FIG.4.6 (b)

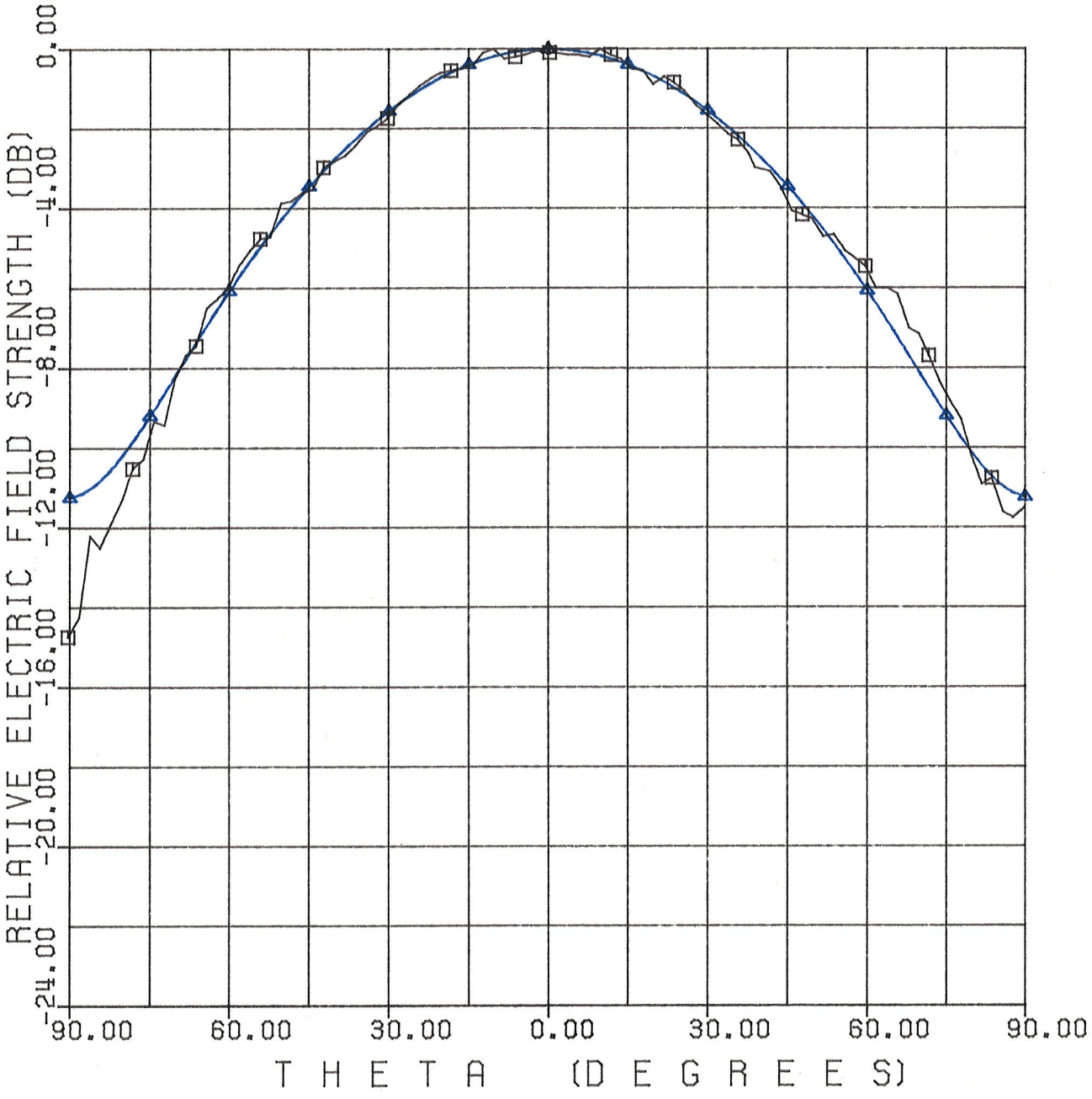

FIGURE 4. 9: COMPARISON OF THE EXPERIMENTAL AND THE NUMERICAL DATA ; $E_{\phi}(\theta)$ FR = 2.2 GHZ , ϕ = 90° AND = 270°

□ EXPERIMENTAL

△ NUMERICAL; SEGMENTATION BASED ON FIG.4.6 (b)

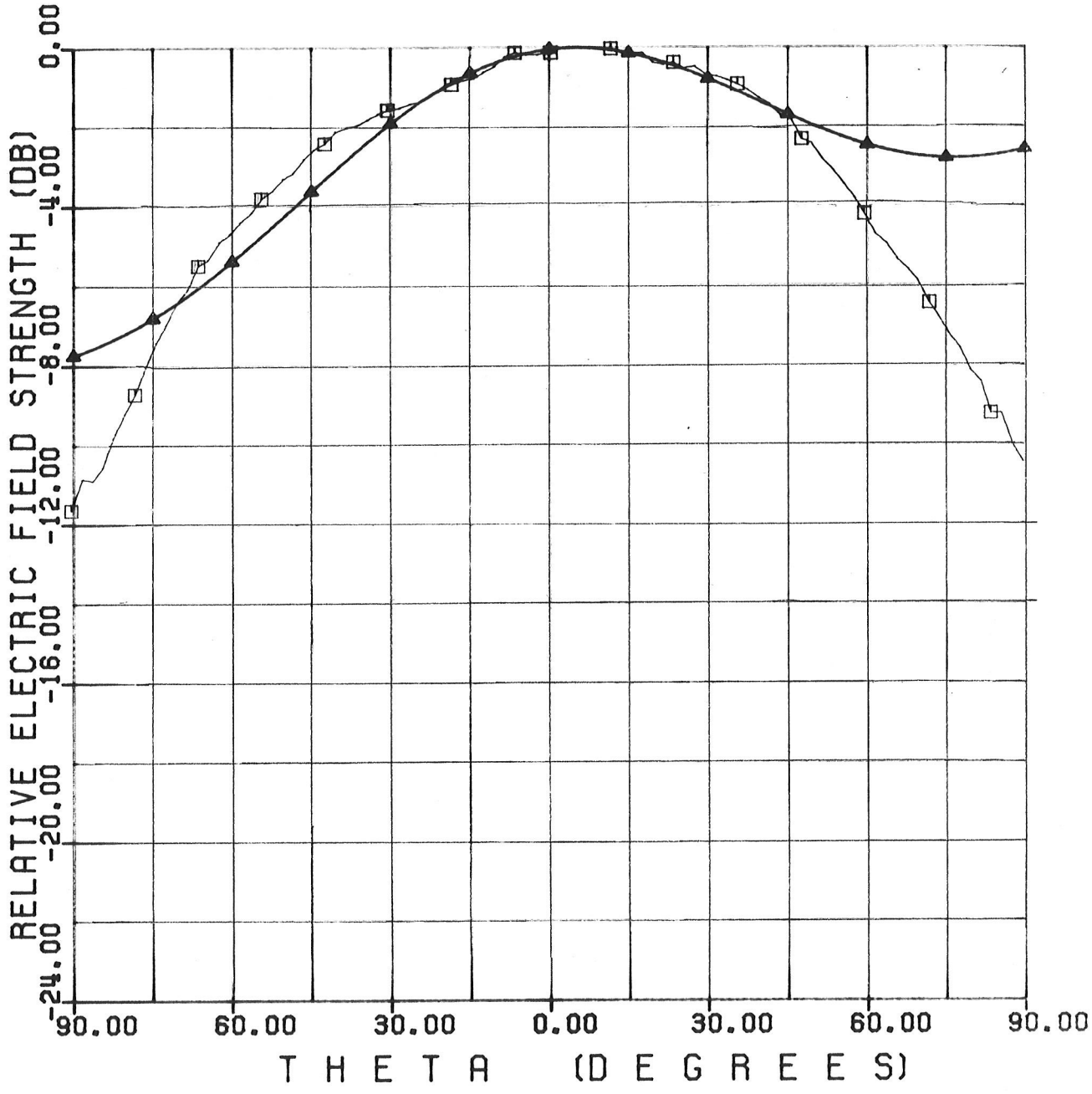

FIGURE 4.10 : COMPARISON OF THE EXPERIMENTAL AND THE NUMERICAL DATA ; $E_\theta(\theta)$, FR = 2.0 GHZ , ϕ = 0° AND 90°

⊡ EXPERIMENTAL

▲ NUMERICAL ; SEGMENTATION BASED ON FIG.4.6 (b)

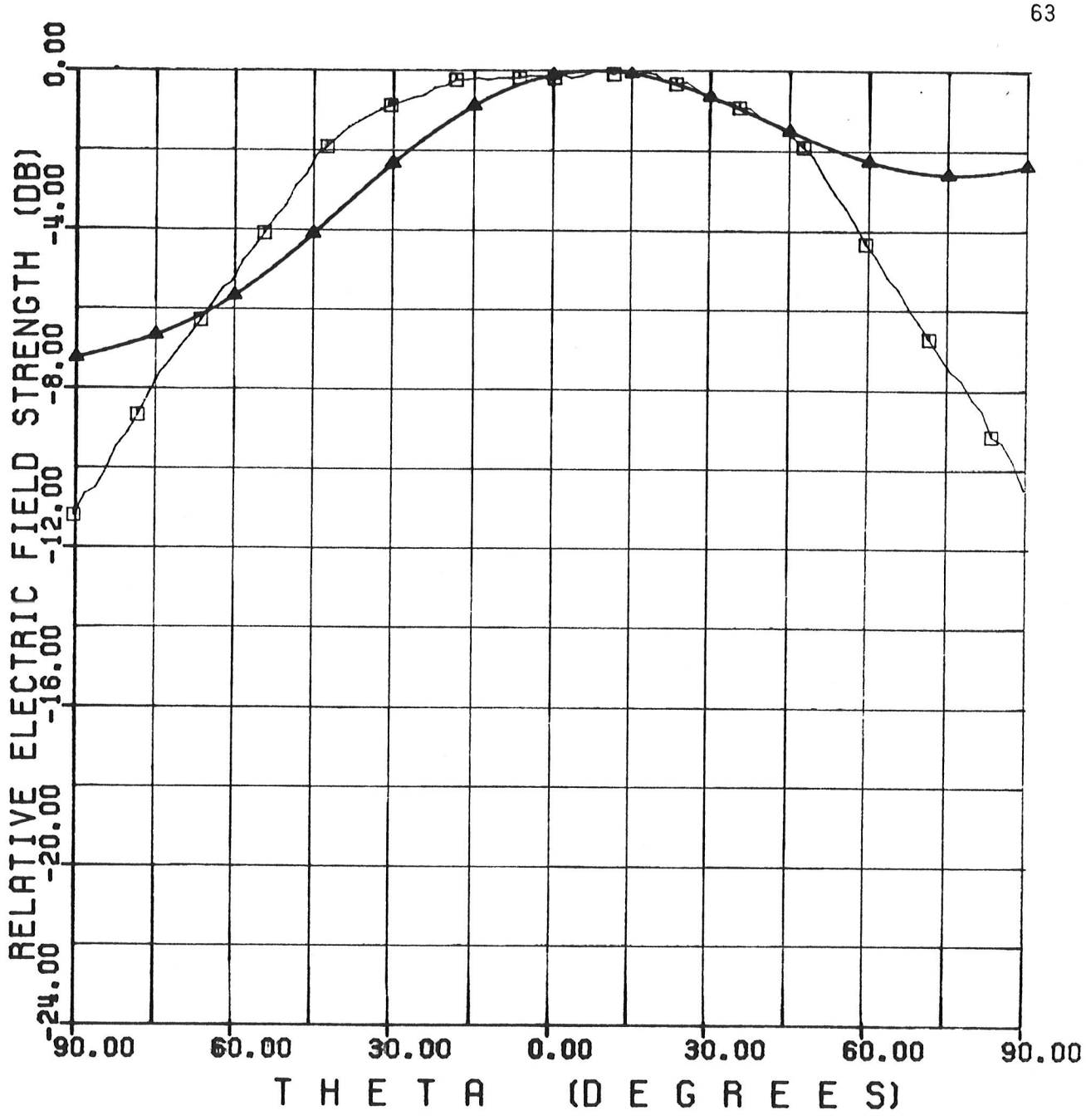

FIGURE 4.11: COMPARISON OF THE EXPERIMENTAL AND THE NUMERICAL DATA ; $E_\theta(\theta)$, FR = 2.1 GHZ , ϕ = 0° AND 90°

□ EXPERIMENTAL

▲ NUMERICAL; SEGMENTATION BASED ON FIG.4.6 (b)

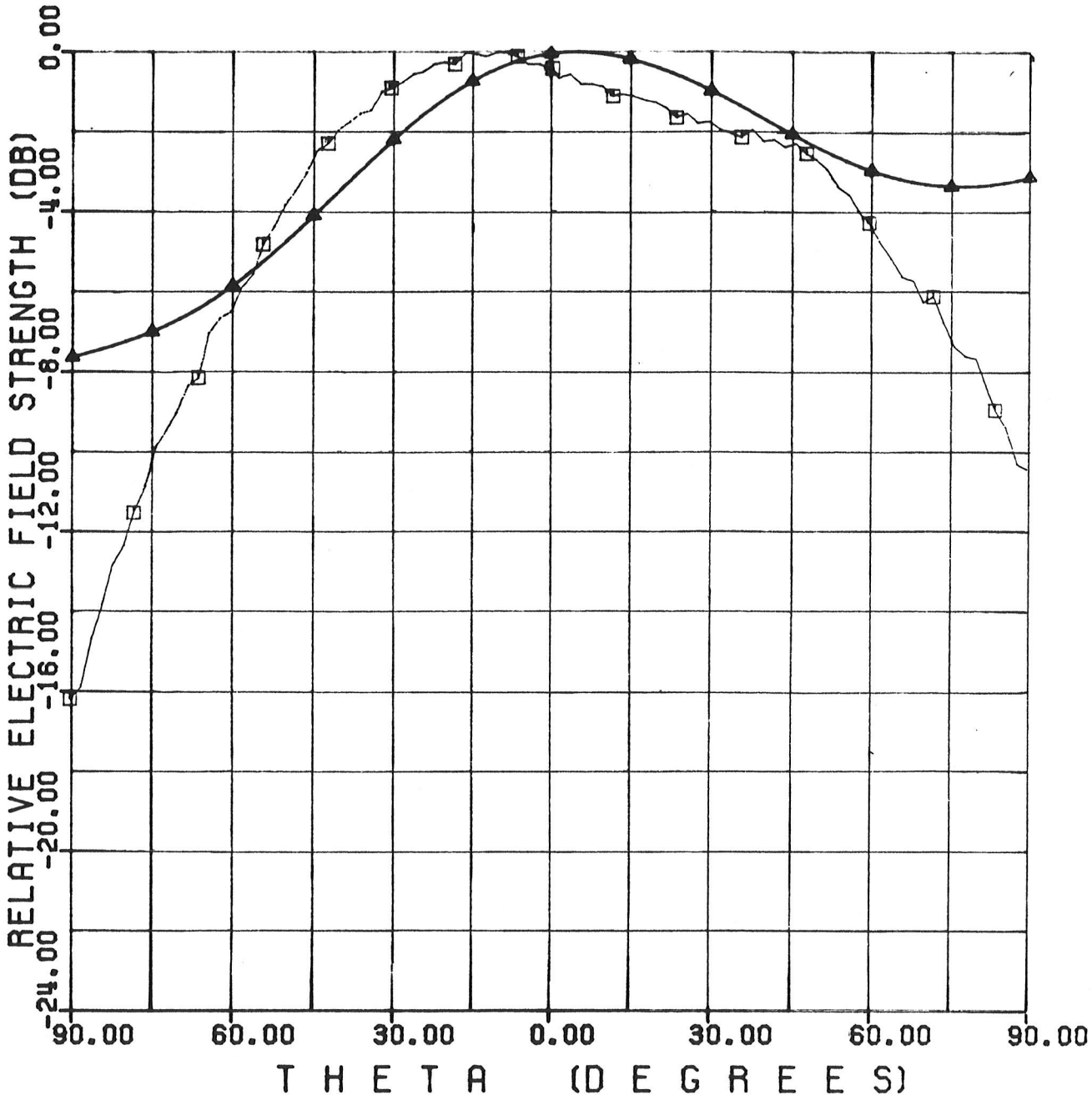

FIGURE 4.12: COMPARISON OF THE EXPERIMENTAL AND THE NUMERICAL DATA ; $E_\theta(\theta)$, FR = 2.2 GHZ , ϕ = 0° AND 90°

□ EXPERIMENTAL

▲ NUMERICAL; SEGMENTATION BASED ON FIG.4.6 (b)

4.3 COMPARISON WITH TRANSMISSION LINE MODELING

For additional verification of the radiation patterns calculated by the present method, they are also compared with patterns calculated by the transmission line models [1] and [2].

Figs 4.13-18 illustrate the comparison at three frequencies in two principal planes. The segmentation for the antenna modeling is shown in Fig.4.6 (b).

This comparison show that the results obtained by present method is more accurate than the results obtained by transmission line model, especially for $E_{\phi}(\theta)$. For $E_{\theta}(\theta)$, the calculated patterns are mostly between the measured patterns and the patterns based on the transmission line model.

The comparison indicates that the present method can give a better prediction than the transmission line model.

The results could also be compared with those of the modal expansion method. However, when only the lowest modes are selected its results become identical to those of the transmission line model. For this reason, such a comparison is not attempted.

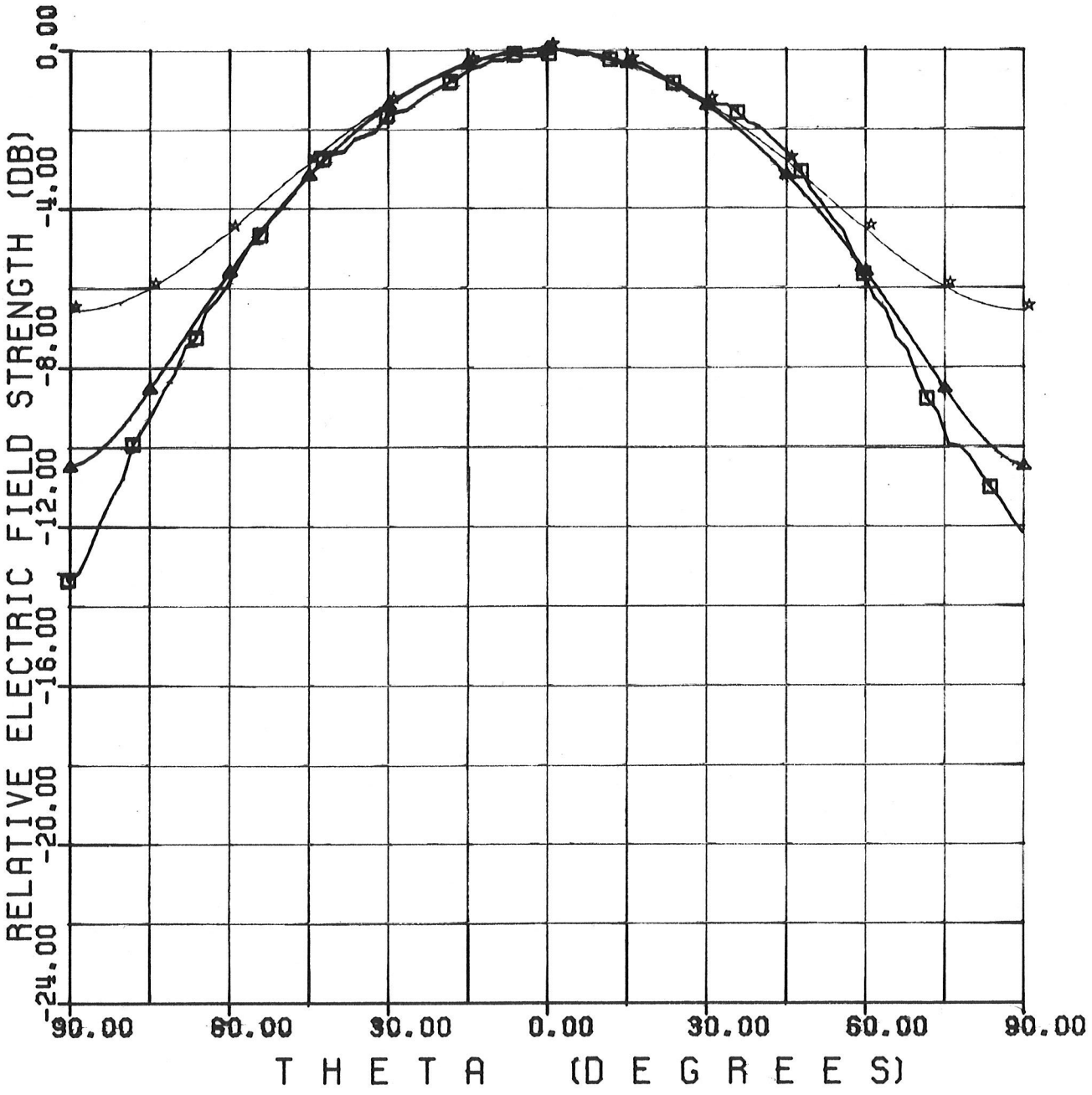

FIGURE 4.13: COMPARISON WITH THE TRANSMISSION LINE MODEL

$E_\phi(\theta)$ FR = 2.0 GHZ , φ = 90° AND = 270°

□ EXPERIMENTAL

△ NUMERICAL ; SEGMENTATION BASED ON FIG.4.6 (b)

★ TRANSMISSION LINE MODEL

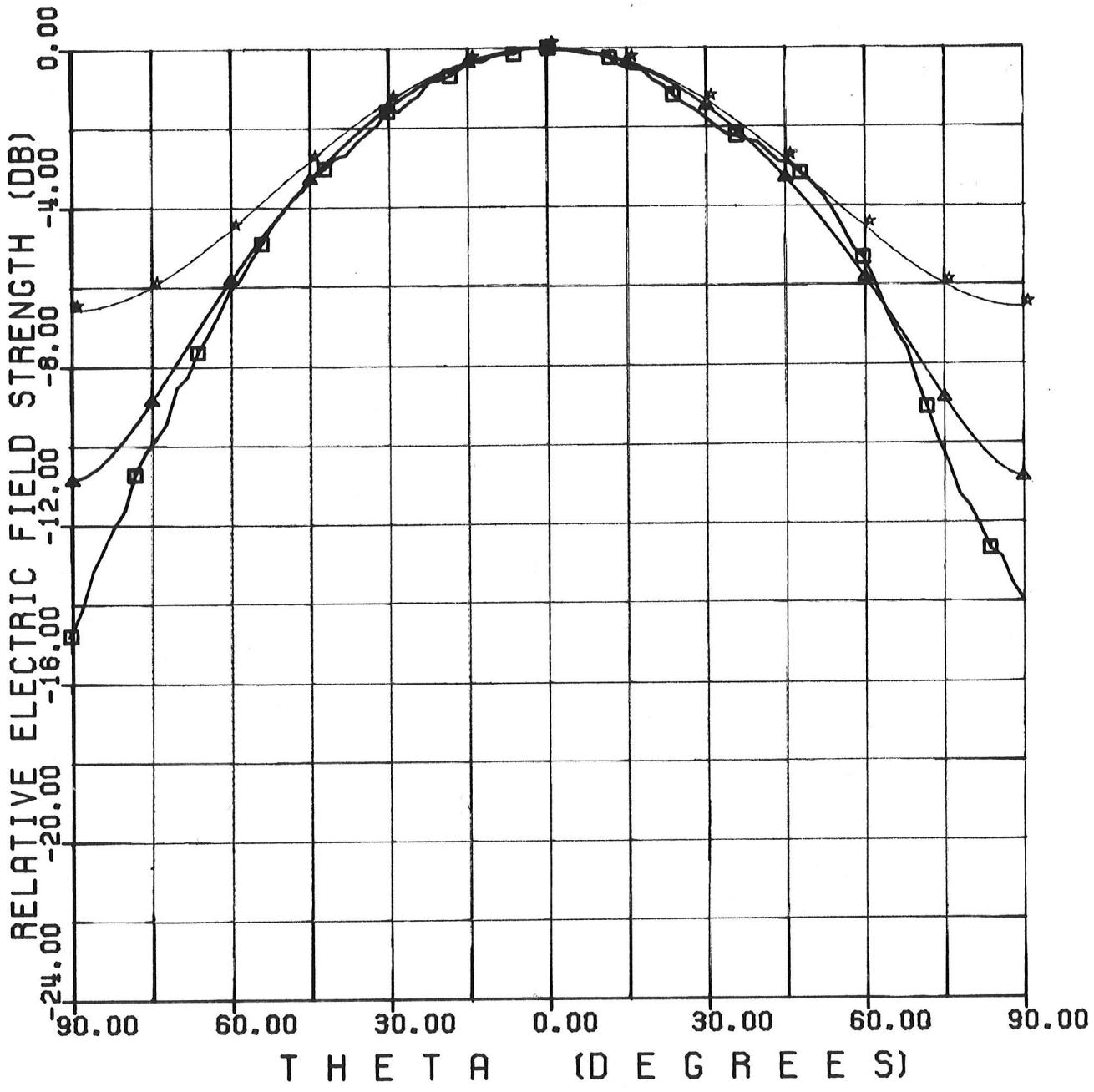

FIGURE 4.14: COMPARISON WITH THE TRANSMISSION LINE MODEL

$E_\varphi(\theta)$ FR = 2.1 GHZ , φ = 90° AND = 270°

□ EXPERIMENTAL

△ NUMERICAL; SEGMENTATION BASED ON FIG.4.6 (b)

★ TRANSMISSION LINE MODEL

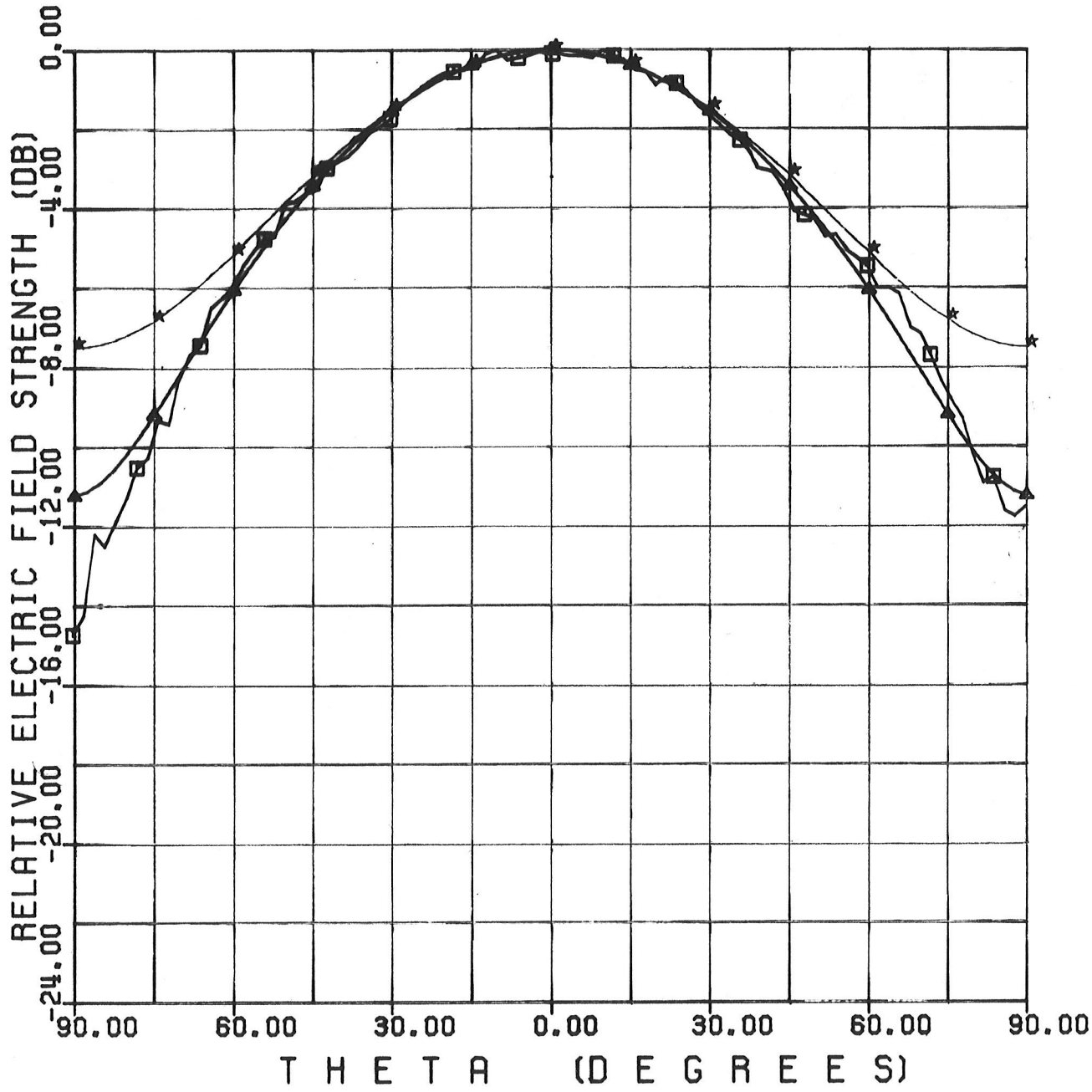

FIGURE 4.15: COMPARISON WITH THE TRANSMISSION LINE MODEL

$E_\varphi(\theta)$ FR = 2.2 GHZ , φ = 90° AND = 270°

□ EXPERIMENTAL

△ NUMERICAL ; SEGMENTATION BASED ON FIG.4.6 (b)

★ TRANSMISSION LINE MODEL

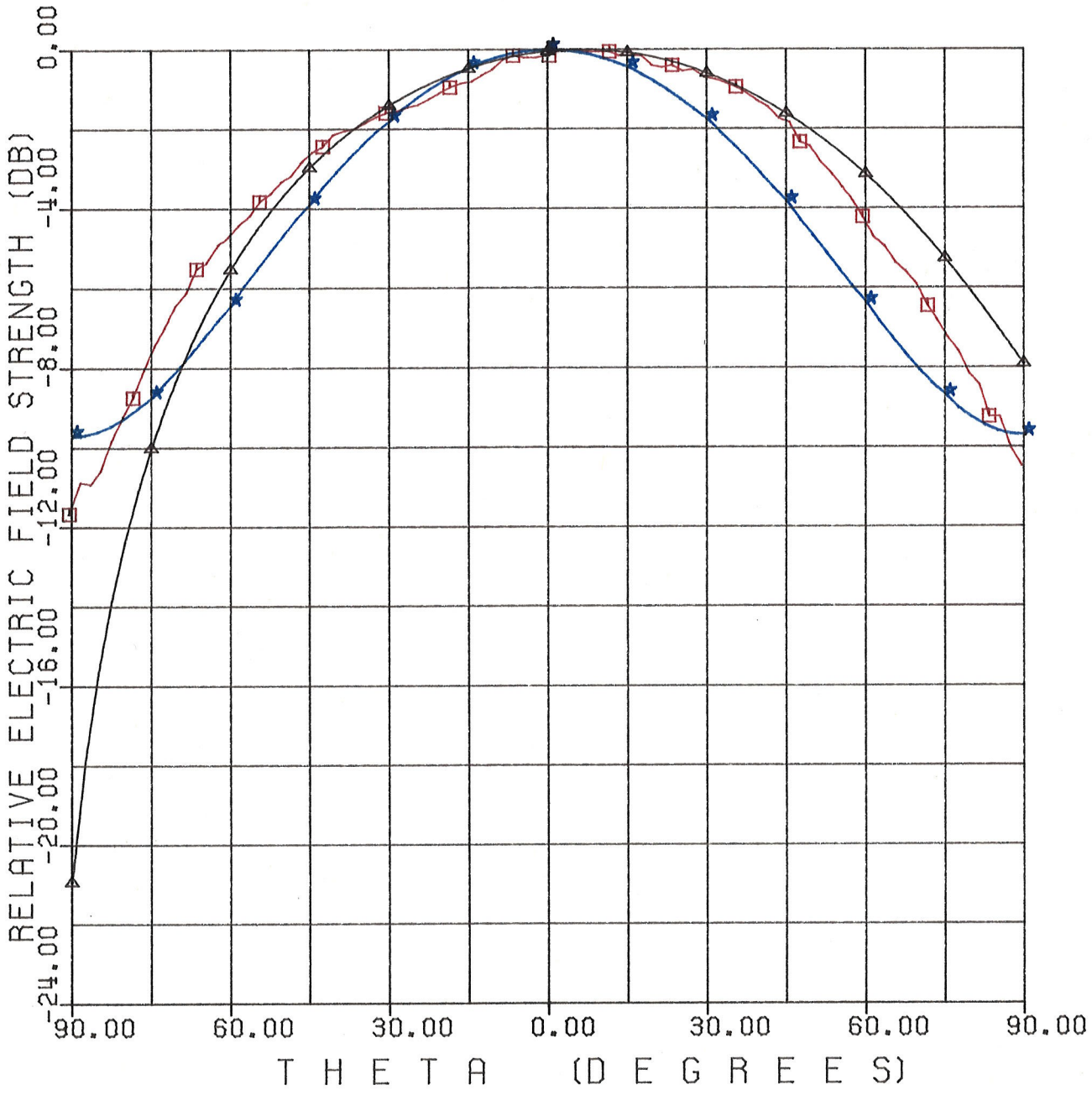

FIGURE 4.16: COMPARISON OF THE EXPERIMENTAL AND THE NUMERICAL DATA ; $E_\theta(\theta)$, FR = 2.0 GHZ , ϕ = 0° AND 90°

□ EXPERIMENTAL

△ NUMERICAL; SEGMENTATION BASED ON FIG.4.6 (c)

★ TRANSMISSION LINE MODEL

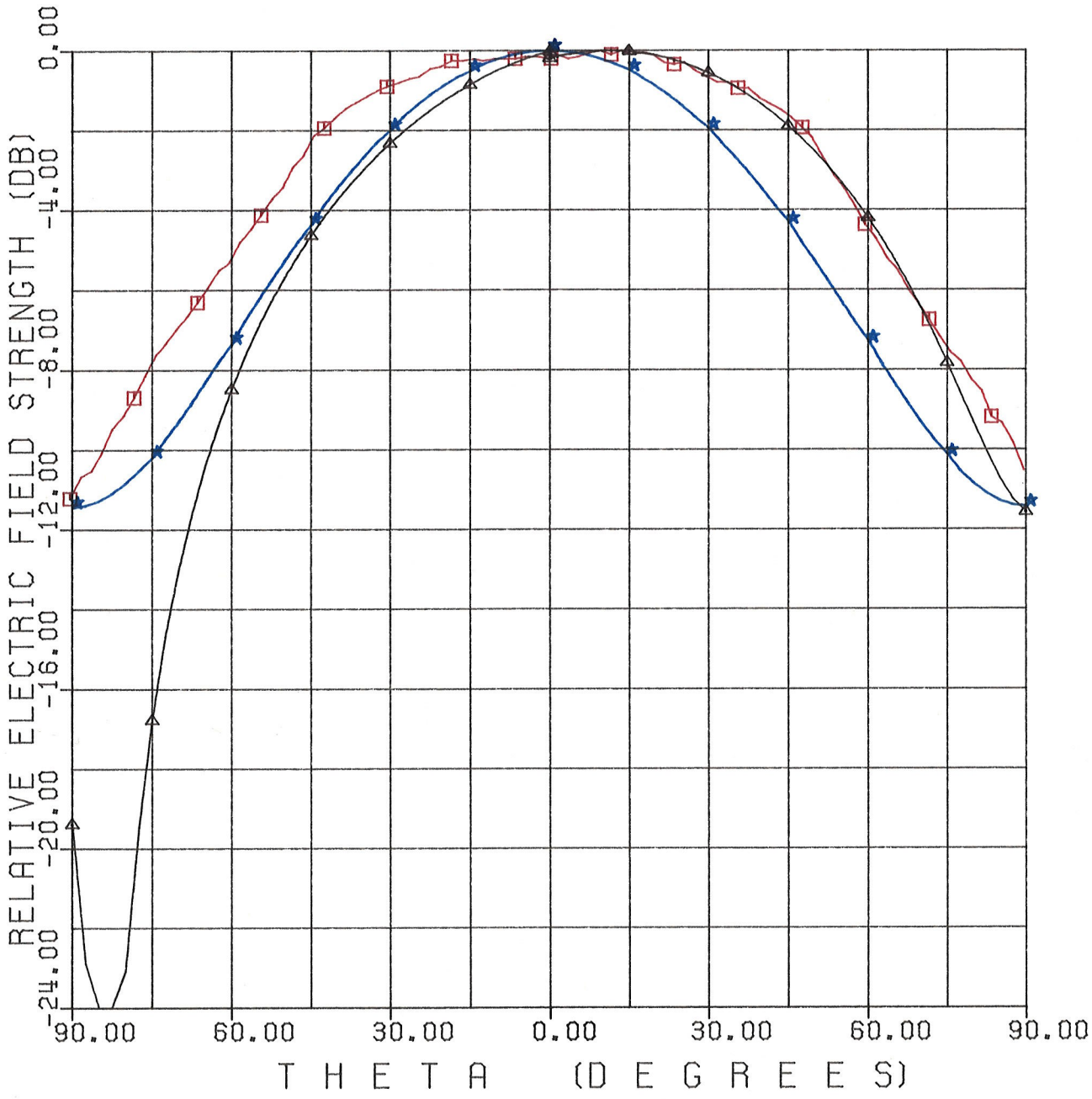

FIGURE 4.17: COMPARISON OF THE EXPERIMENTAL AND THE NUMERICAL DATA ; $E_{\theta}(\theta)$, FR = 2.1 GHZ , ϕ = 0° AND 90°

□ EXPERIMENTAL

△ NUMERICAL; SEGMENTATION BASED ON FIG.4.6 (b)

☆ TRANSMISSION LINE MODEL

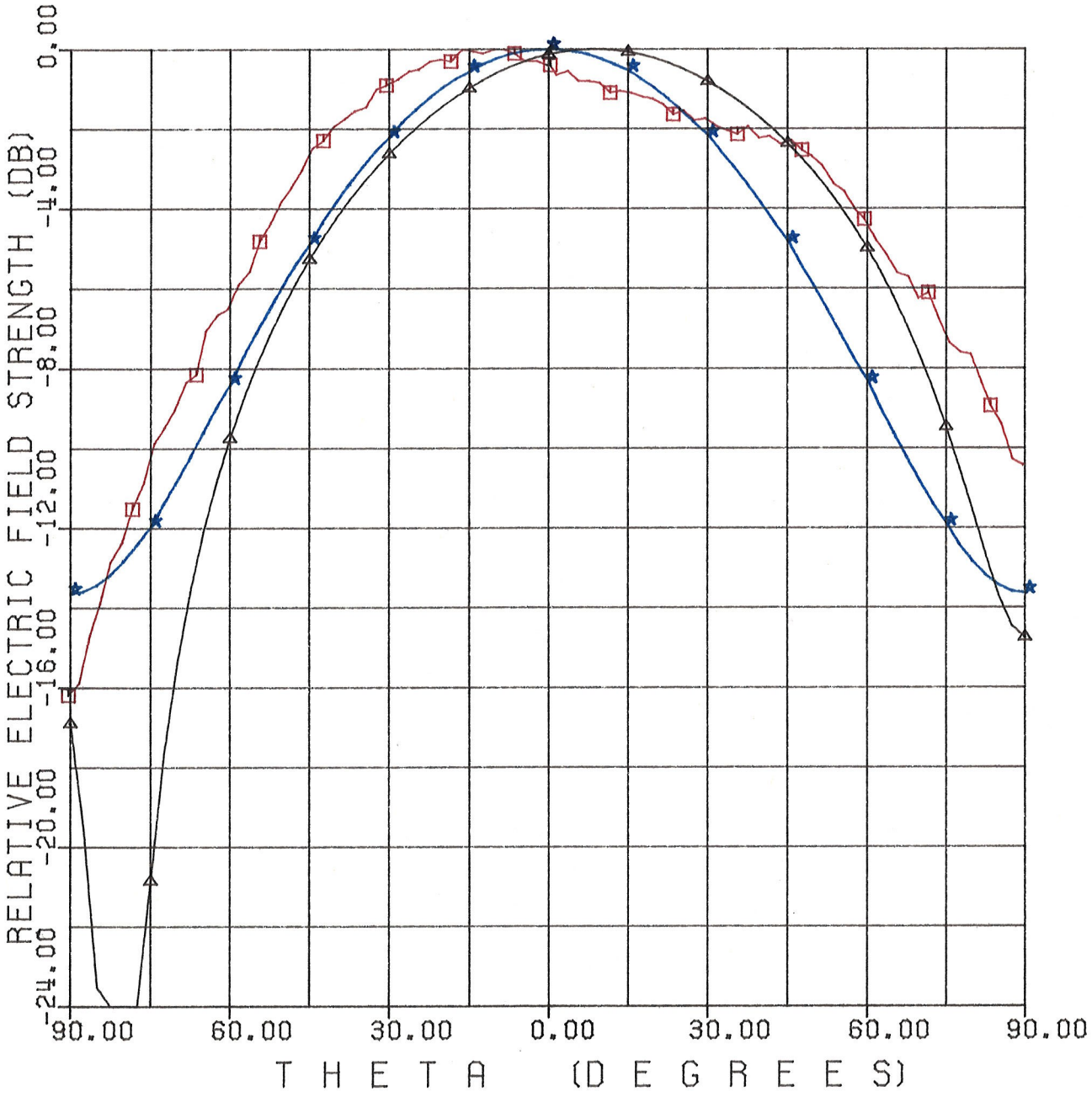

FIGURE 4.18: COMPARISON OF THE EXPERIMENTAL AND THE NUMERICAL DATA ; $E_\theta(\theta)$, FR = 2.2 GHZ , ϕ = 0° AND 90°

□ EXPERIMENTAL

△ NUMERICAL; SEGMENTATION BASED ON 4.6 (b)

☆ TRANSMISSION LINE MODEL

4.4 EFFECT OF SURFACE SEGMENTATION

It is known that numerical results normally converge to the exact solution by expanding the series of basic functions to infinity [18]. Practically, a good numerical approach should not only give accurate results, it should also converge quickly.

To study the convergence of the present method, a comparison between the results of three different segmentations is shown in Figs 4.19-22. The segmentations are illustrated in Fig.4.6. In Fig.4.6 (a) the subpatch dimensions are $\lambda_g/4$ and $\lambda_g/8$ on the conductor and the dielectric, respectively. While in Fig.4.6 (b) and (c) the subpatches are the same size on both conductor and dielectric and are of size $\lambda_g/6$ and $\lambda_g/12$, respectively.

In the first three figures 4.19-4.21, the patterns based on Figs 4.6 b and c are almost identical with each other and very close to the measured ones over the most range of θ. In Fig.4.22 the calculated patterns are converging to the measured ones as the sizes of the subpatches are decreased. This implies that the numerical results converge rapidly to the exact solution. Thus for acceptable results, the side dimensions of each subpatch need not be less than 0.125 λ_g.

This means, if, the dimensions of the conducting patch of a microstrip antenna are $0.5\lambda_g \times 0.5\lambda_g$, accurate solutions can be obtained by taking the segmentation as shown in Fig.4.6 (b). Such a segmentation results in 144 unknowns and will

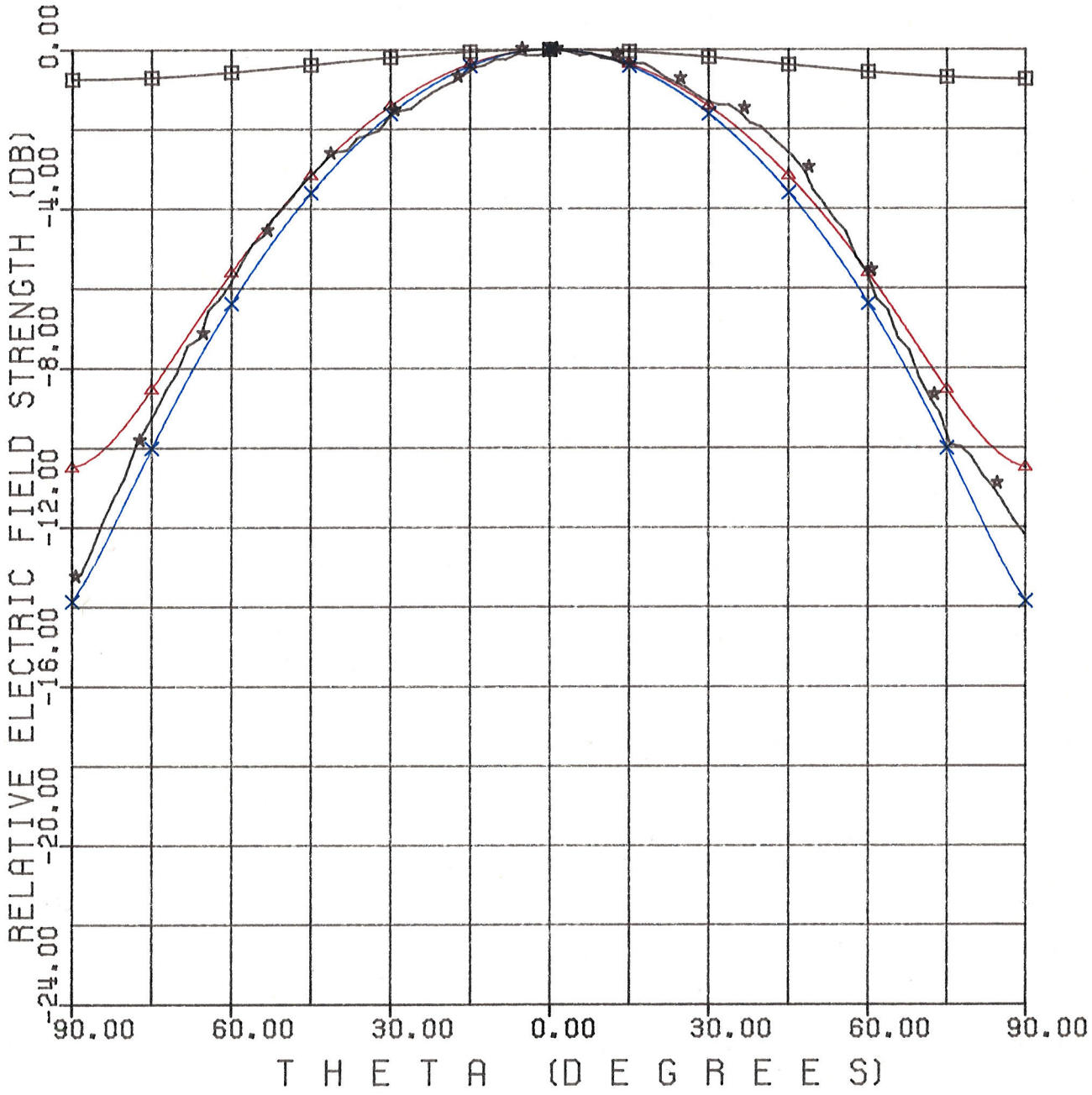

FIGURE 4.19: THE EFFECT OF THE NUMBER AND SIZE OF THE DIVISIONS

□ RADIATION PATTERN DUE TO 4 DIVISIONS ON PATCH

△ RADIATION PATTERN DUE TO 16 DIVISIONS ON PATCH

× RADIATION PATTERN DUE TO 36 DIVISIONS ON PATCH

★ RADIATION PATTERN OBTAINED FROM MEASUREMENT

$E_{\varphi}(\theta)$; FR = 2.0 GHZ , ϕ = 90° AND 270°

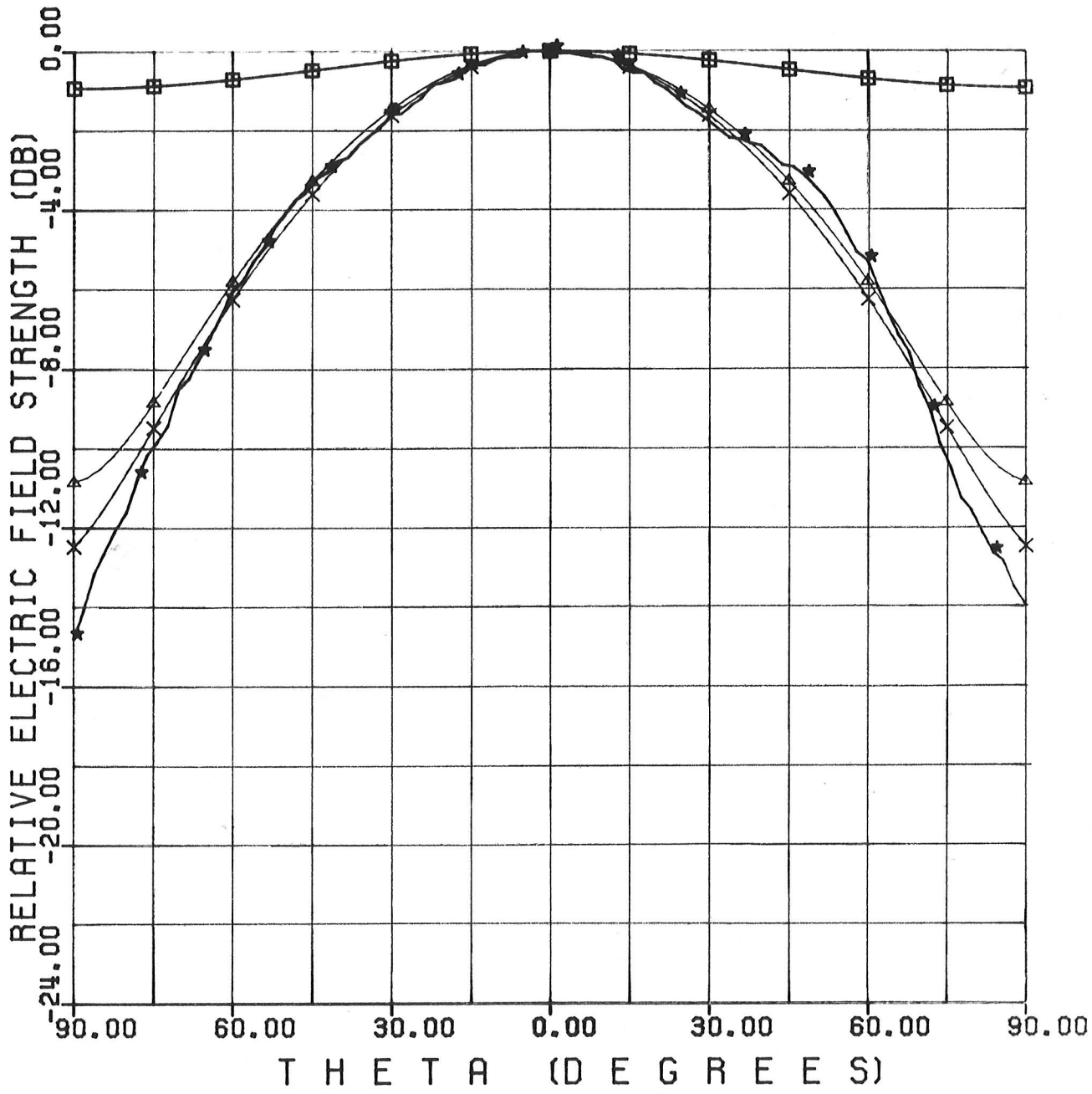

FIGURE 4.20: THE EFFECT OF THE NUMBER AND SIZE OF THE DIVISIONS

□ RADIATION PATTERN DUE TO 4 DIVISIONS ON PATCH

▲ RADIATION PATTERN DUE TO 16 DIVISIONS ON PATCH

× RADIATION PATTERN DUE TO 36 DIVISIONS ON PATCH

★ RADIATION PATTERN OBTAINED FROM MEASUREMENT

$E_{\phi}(\theta)$; FR = 2.1 GHZ , ϕ = 90° AND 270°

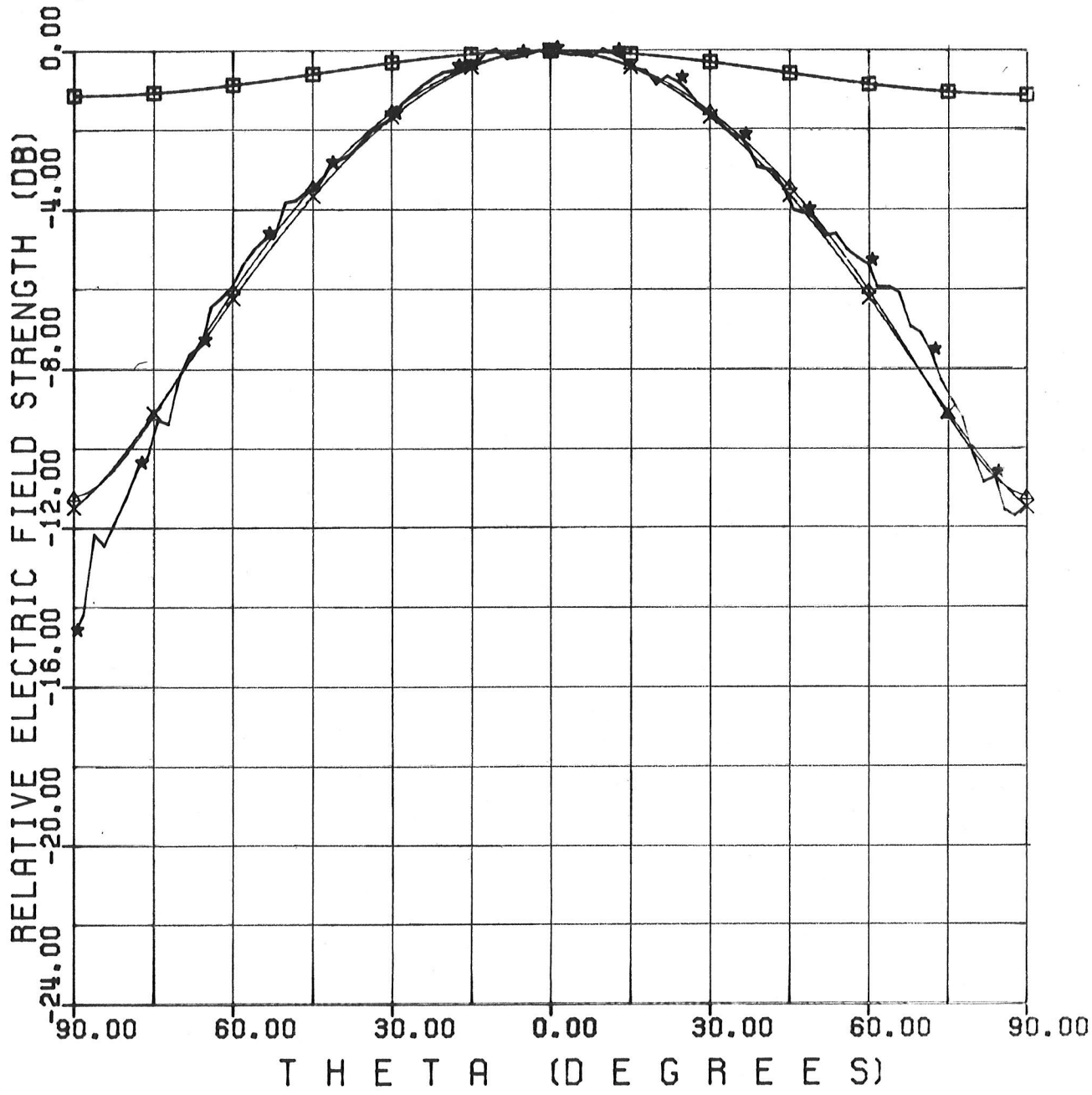

FIGURE 4.21: THE EFFECT OF THE NUMBER AND SIZE OF THE DIVISIONS

□ RADIATION PATTERN DUE TO 4 DIVISIONS ON PATCH

△ RADIATION PATTERN DUE TO 16 DIVISIONS ON PATCH

× RADIATION PATTERN DUE TO 36 DIVISIONS ON PATCH

★ RADIATION PATTERN OBTAINED FROM MEASUREMENT

$E_\phi(\theta)$; FR = 2.2 GHZ , ϕ = 90° AND 270°

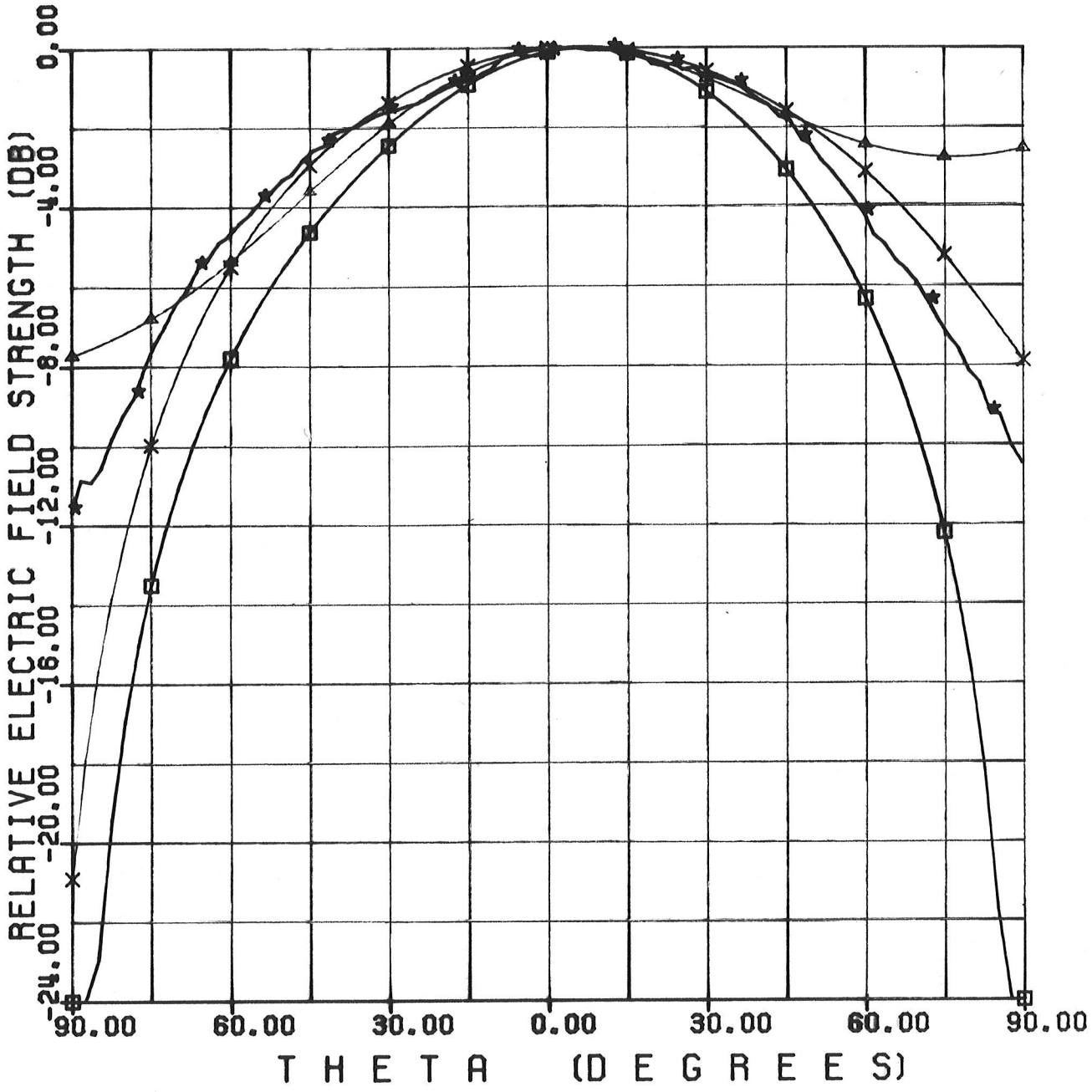

FIGURE 4.22: THE EFFECT OF THE NUMBER AND SIZE OF THE DIVISIONS

□ RADIATION PATTERN DUE TO 4 DIVISIONS ON PATCH

▲ RADIATION PATTERN DUE TO 16 DIVISIONS ON PATCH

× RADIATION PATTERN DUE TO 36 DIVISIONS ON PATCH

★ RADIATION PATTERN OBTAINED FROM MEASUREMENT

$E_\theta(\theta)$: FR = 2.0 GHZ , ϕ = 0° AND 90°

involve the solution of 144 linear equations, which is not an unreasonable number for numerical computation. Table 1 lists the required computation time and storage for determining the field distributions.

TABLE 1

No .of Unknowns	CPU Time	Memory Size
96	5.1 sec	190 k
144	17.2 sec	436 k
400	290 sec	2625 k

According to the above discussion, one can say that the electromagnetic field integral equations developed in this thesis not only give accurate results, but also converge fast. They can therefore be used in the numerical solution of similar problem involving microstrip antennas.

As mentioned in Section 2.4.3, the numerical solutions by utilizing different combination of integral equations, for the field points on both sides of the conducting patch, are not same, i.e., for four combinations, the results are not unique, as Mautz and Harrington have indicated in [22]. Our numerical solutions have verified this point. As an example, Figs 4.23-24 show the results for the numerical data which

is obtained by using the electric - field equations for the field points on both sides of the conductor patch. One can see that in all three cases the results are worse than those of the previous cases.

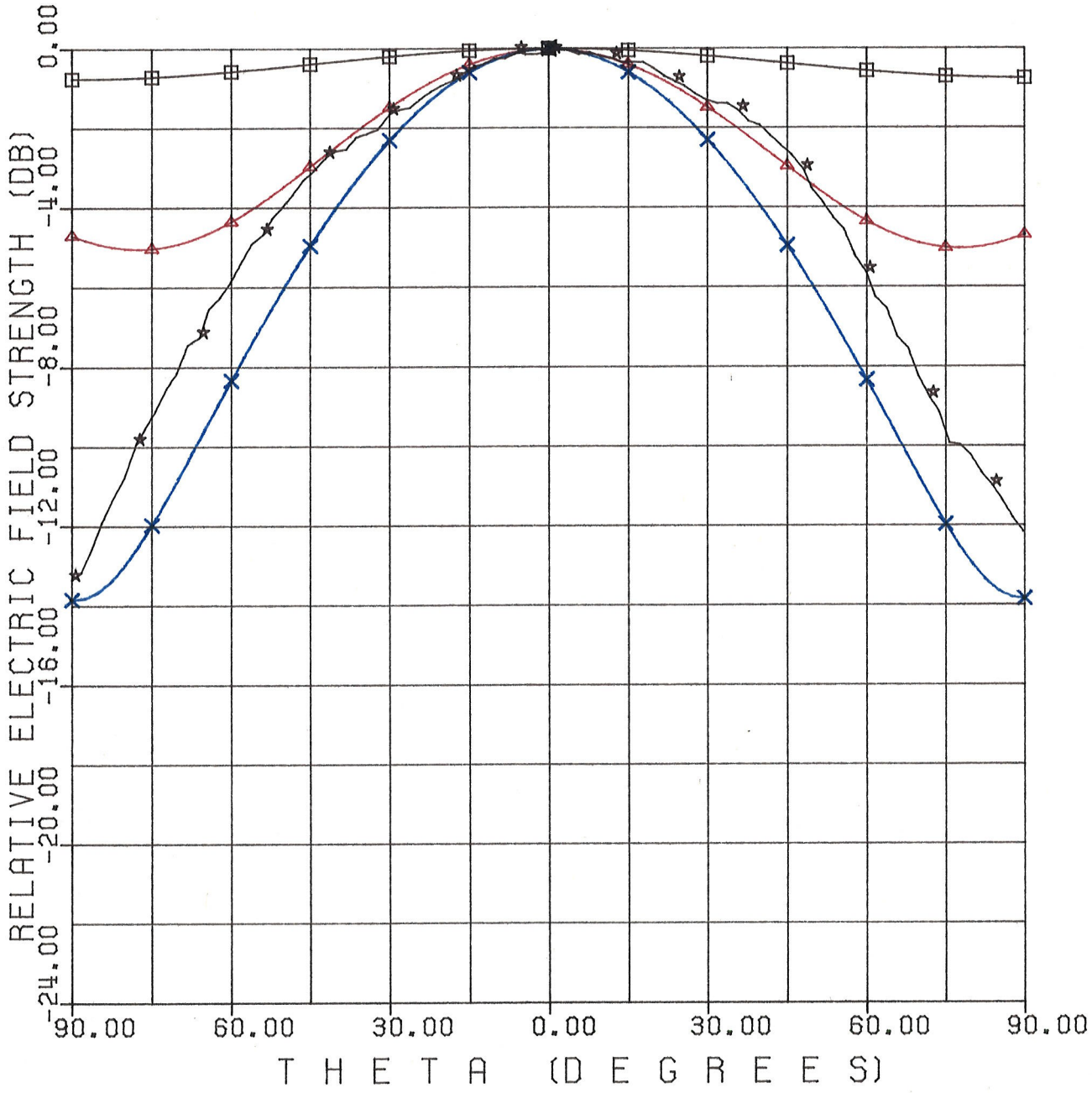

FIGURE 4.23: THE EFFECT OF THE NUMBER AND SIZE OF THE DIVISIONS

□ RADIATION PATTERN DUE TO 16 DIVISIONS ON APERTURE

△ RADIATION PATTERN DUE TO 36 DIVISIONS ON APERTURE

× RADIATION PATTERN DUE TO 100 DIVISIONS ON APERTURE

☆ RADIATION PATTERN OBTAINED FROM MEASUREMENT

$E_\phi(\theta)$; FR = 2.0 GHZ , ϕ = 90° AND 270° , W = L = $\lambda g/2$.

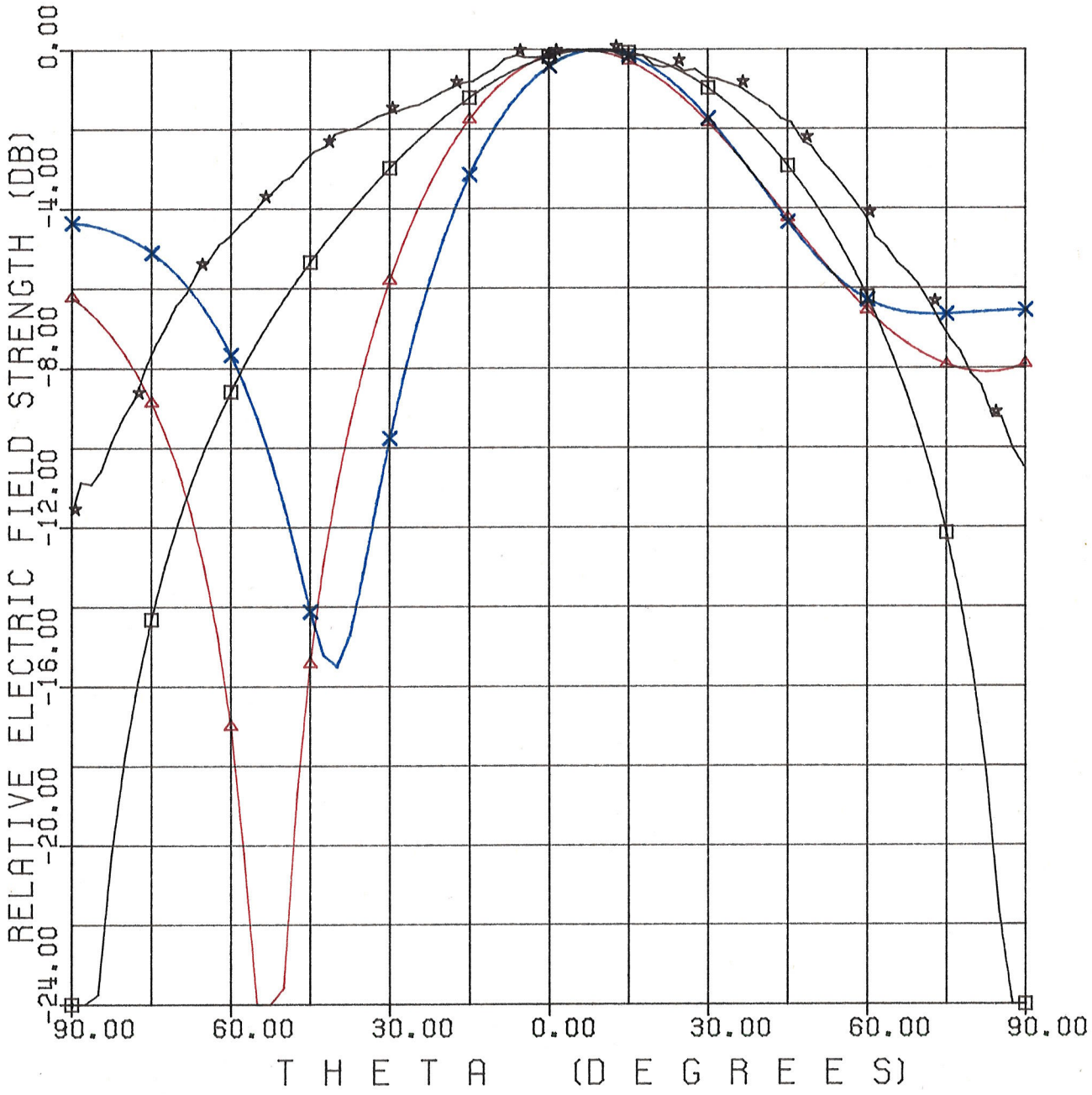

FIGURE 4.24: THE EFFECT OF THE NUMBER AND SIZE OF THE DIVISIONS

□ RADIATION PATTERN DUE TO 36 DIVISIONS ON APERTURE

△ RADIATION PATTERN DUE TO 64 DIVISIONS ON APERTURE

× RADIATION PATTERN DUE TO 100 DIVISIONS ON APERTURE

★ RADIATION PATTERN OBTAINED FROM MEASUREMENT

$E_\theta(\theta)$; FR = 2.0 GHZ , ϕ = 0° AND 90°, W = L = $\lambda_g/2$.

Chapter V

CONCLUSION

This thesis has presented a new technique for numerical solution of problems involving microstrip antenna using the moment method. We have shown that the electric and magnetic field integral equations developed here connect the interior and exterior fields of the conducting patch. The dielectric substrate are accounted for by these field integral equations. The equations are suitable for a wide variety of expansion functions and avoid the boundary line integral. The radiation patterns for the square half-wavelehgth patch antennas obtained by this technique are substantiated by the empirical data and are more accurate than those obtained by previous approximation methods. The numerical results show that the formulations and the computer program based on this technique are efficient and a powerful tool for studying the microstrip antennas. It is apparent that the technique can be easily used to examine other three-dimensional problem. The method can also be used to investigate other shape microstrip antennas. All of these studies, including the near field characteristics, are left for future investigations.

Appendix A

THE DERIVATION OF EQUATIONS (3.12) - (3.15)

In rectangular coordinates using the ∇' operator, we can show that:

$$\frac{\partial \Phi}{\partial x'} = \left(jk + \frac{1}{R} \right) \Phi \frac{X}{R} \tag{A.1}$$

Assuming

$$N = \left(jk + \frac{1}{R} \right) \tag{A.2}$$

Then,

$$\frac{\partial \Phi}{\partial x'} = N \Phi \frac{X}{R} \tag{A.3}$$

Similarly, we have

$$\frac{\partial \Phi}{\partial y} = N \Phi \frac{Y}{R} \tag{A.4}$$

and

$$\frac{\partial \Phi}{\partial z'} = N \Phi \frac{Z}{R} \tag{A.5}$$

So,

$$\nabla'\Phi = N\,\Phi\,\frac{1}{R}\,(X\hat{i} + Y\hat{j} + Z\hat{k}) \tag{A.6}$$

For different k_0 and k_i,

$$N_e = (jk_0 + \frac{1}{R}) \tag{A.7}$$

$$N_i = (jk_i + \frac{1}{R}) \tag{A.8}$$

Now, we derive the functions M_i, M_e, A_i, A_e, B_i, B_e, C_i, C_e, D_i, and D_e.

First, we derive the operation $(\hat{n} \times \bar{H})$

$$\hat{n} \times H = \hat{k} \times (H_x\hat{i} + H_y\hat{j} + H_z\hat{k})$$

$$= H_x\hat{j} - H_y\hat{i} \tag{A.9}$$

and

$$(H_x\hat{j} - H_y\hat{i}) \cdot (\hat{i}\frac{\partial}{\partial x'} + \hat{j}\frac{\partial}{\partial y'} + \hat{k}\frac{\partial}{\partial z'})$$

$$= -H_y\frac{\partial}{\partial x'} + H_x\frac{\partial}{\partial y'} \tag{A.10}$$

Second, we derive $\frac{\partial}{\partial x}\nabla\Phi$ and $\frac{\partial}{\partial y}\nabla\Phi$. Applying (A.4), we obtain

$$= [\, M X (X \hat{i} + Y \hat{j} + Z \hat{k}) + N \hat{i} \,] \frac{\Phi}{R} \qquad (A.11)$$

where

$$M = \frac{k^2}{R} + \frac{3jk}{R^2} - \frac{1}{R^3} \qquad (A.12)$$

For different k_0 and k_i, we have

$$M_e = \frac{k_e^2}{R} - \frac{3jk_e}{R^2} - \frac{1}{R^3} \qquad (A.13)$$

$$M_i = \frac{k_i^2}{R} - \frac{3jk_i}{R^2} - \frac{1}{R^3} \qquad (A.14)$$

Similarly, we obtain

$$\frac{\partial}{\partial y'} \nabla' \Phi = [\, M Y (X \hat{i} + Y \hat{j} + Z \hat{k}) + N \hat{j} \,] \frac{\Phi}{R} \qquad (A.15)$$

and

$$\frac{\partial}{\partial z'} \nabla' \Phi = [\, M Z (X \hat{i} + Y \hat{j} + Z \hat{k}) + N \hat{k} \,] \frac{\Phi}{R} \qquad (A.16)$$

Applying (A.6),(A.7),(A.8),(A.11),(A.13),(A.14),(A.15), and (A.16) to equation (2.39) and (2.40), we obtain:

$$0 = 2E_y^{inc} - \frac{1}{2\pi} \int_{S_e} [j\omega\mu \, (\Phi_e - A_e) H_{ex} - j\omega\mu B_e H_{ey}] \, ds'$$

$$- \frac{1}{2\pi} \int_{S_i} [j\omega\mu \, (\Phi_i - A_i) H_{ix} - j\omega\mu B_i H_{iy}] \, ds'$$

$$- \frac{1}{2\pi} \int_{S_{ed}} [\, j\omega\mu \, (\Phi_e - A_e + \Phi_i - A_i) \, H_{ex}$$

$$+ j\omega\mu \, (B_e + B_i) \, H_{ey} + (D_e + D_i) \, E_{ey}] \, ds' + \int_{S_{ec}^i} \{ f \, (H_{ex}^i ,$$

$$H^i_{ey}, H^i_{ix}, H^i_{iy})\, ds' + \int_{S^i_{ed}} f\,(H^i_{ex}, H^i_{ey}, E^i_{ex}, E^i_{ey})\, ds' \qquad \textbf{(A.17)}$$

and for H

$$0 = 2H_y^{inc} - \frac{1}{2\pi}\int_{S_{ec}} D_e H_{ey}\, ds' - \frac{1}{2\pi}\int_{S_{ic}} D_i H_{iy}\, ds' - \frac{1}{2\pi}\int_{S_{ed}} \{[\, j\omega\varepsilon_0 (\Phi_e - A_e) + j\omega\varepsilon\,(\Phi_i - A_i)]\, E_{ex} + (j\omega\varepsilon_0 B_e + j\omega\varepsilon\, B_i)\, E_{ey} + (D_e + D_i)\, H_{ey}\}\, ds' + \int_{S^i_{ec}} f\,(H^i_{ey}, H^i_{iy}, H^i_{ex}, H^i_{ix})\, ds' + \int_{S^i_{ed}} f\,(H^i_{ex}, H^i_{ey}, E^i_{ex}, E^i_{ey})\, ds' \qquad \textbf{(A.18)}$$

for X - direction;

$$0 = -2E_x^{inc} + \frac{1}{2\pi}\int_{S_{ec}} [j\omega\mu\, B_e H_{ey} - j\omega\mu\,(\Phi_e - C_e) H_{ex}]\, ds' + \frac{1}{2\pi}\int_{S_{ic}} [j\omega\mu\, B_i H_{iy} - j\omega\mu\,(\Phi_i - C_i) H_{ix}]\, ds' - \frac{1}{2\pi}\int_{S_{ed}} [\, j\omega\mu\,(\Phi_e - C_e + \Phi_i - A_i)\, H_{ey} + j\omega\mu\,(B_e + B_i)\, H_{ex} + (D_e + D_i)\, E_{ex}]\, ds' + \int_{S^i_{ec}} f\,(H^i_{ex}, H^i_{ey}, H^i_{ix}, H^i_{iy})\, ds' + \int f\,(H^i_{ex}, H^i_{ey}, E^i_{ex}, E^i_{ey})\, ds' \qquad \textbf{(A.19)}$$

and,

$$0 = -2H_x^{inc} - \frac{1}{2\pi}\int_{S_{ec}} D_e H_{ex}\,ds' - \frac{1}{2\pi}\int_{S_{ic}} D_i H_{ix}\,ds' + \frac{1}{2\pi}\int_{S_{ed}}\{(D_e + D_i)\,H_{ex}$$

$$+ [-j\omega\varepsilon_0(\Phi_e - C_e) + j\omega\varepsilon\,(\Phi_i - C_i)]\,E_{ey} + (j\omega\varepsilon_0 B_e + j\omega\varepsilon\, B_i)\,E_{ex}\}\,ds'$$

$$+ \int_{S_{ec}^i} f\,(H_{ex}^i, H_{ey}^i, H_{ix}^i, H_{iy}^i)\,ds' + \int_{S_{ed}^i} f\,(H_{ex}^i, H_{ey}^i, E_{ex}^i, E_{ey}^i)\,ds' \quad \text{(A.20)}$$

for y -direction; where

$$A_e = \frac{\Phi_e}{k_o^2}\left(M_e \frac{Y}{r} + N_e \frac{1}{r}\right) \quad \text{(A.21)}$$

$$A_i = \frac{\Phi_i}{k_i^2}\left(M_i \frac{Y}{r} + N_i \frac{1}{r}\right) \quad \text{(A.22)}$$

$$B_e = \frac{\Phi_e}{k_o^2} M_e \frac{XY}{r} \quad \text{(A.23)}$$

$$B_i = \frac{\Phi_i}{k_i^2} M \frac{XY}{r} \quad \text{(A.24)}$$

$$C_e = \frac{\Phi_e}{k_o}\left(M_e \frac{X}{r} + N_i \frac{1}{r}\right) \quad \text{(A.25)}$$

$$C_i = \frac{\Phi_i}{k_i^2}\left(M_i \frac{X}{r} + N_i \frac{1}{r}\right) \quad \text{(A.26)}$$

$$D_e = \frac{\Phi_e}{k_o^2} N_e Z \tag{A.27}$$

$$D_i = \frac{\Phi_i}{k_i^2} N_i Z \tag{A.28}$$

Appendix B

THE ENTRIES OF THE COEFFICIENT MATRIX

From the equations (3.11)-(3.14) we have the following:

A) On the conducting patch. For the unknown H_{ex},

$$
\begin{aligned}
l_{mn11} &= j\omega\mu \left(A_e - \Phi_e \right) \Delta S \\
l_{mn21} &= - j\omega\mu \, B_e \Delta S \\
l_{mn31} &= 0 \\
l_{mn41} &= D_e \, \Delta S
\end{aligned}
\qquad \text{(B.1)}
$$

For the unknown H_{ey},

$$
\begin{aligned}
l_{mn12} &= - j\omega\mu \, B_e \, \Delta S \\
l_{mn22} &= j\omega\mu \left(C_e - \Phi_e \right) \Delta S \\
l_{mn32} &= - D_e \, \Delta S \\
l_{mn42} &= 0
\end{aligned}
\qquad \text{(B.2)}
$$

For the unknown H_{ix},

$$l_{mn13} = j\omega\mu \left(A_i - \Phi_i \right) \Delta S$$

$$l_{mn23} = - j\omega\mu \, B_i \, \Delta S \qquad \text{(B.3)}$$

$$l_{mn33} = 0$$

$$l_{mn43} = D_i \, \Delta S$$

For the unknown H_{iy},

$$l_{mn41} = - j\omega\mu \, B_i \, \Delta S$$

$$l_{mn42} = j\omega\mu \left(C_i - \Phi_i \right) \Delta S \qquad \text{(B.4)}$$

$$l_{mn43} = - D_i \, \Delta S$$

$$l_{mn44} = 0$$

B) On the dielectric surface. For the unknown H_{ex},

$$l_{mn11} = j\omega\mu \left(A_e - \Phi_e + A_i - \Phi_i \right) \Delta S$$

$$l_{mn21} = - j\omega\mu \left(B_e + B_i \right) \Delta S \qquad \text{(B.5)}$$

$$l_{mn31} = 0$$

$$l_{mn41} = \left(D_e + D_i \right) \Delta S$$

For the unknown H_{ey},

$$l_{mn12} = - j\omega\mu \left(B_e + B_i \right) \Delta S$$

$$l_{mn22} = j\omega\mu \left(C_e - \Phi_e + C_i - \Phi_i \right) \Delta S \qquad \text{(B.6)}$$

$$l_{mn32} = - \left(D_e + D_i \right) \Delta S$$

$$l_{mn42} = 0$$

For the unknown E_{ex},

$$l_{mn13} = 0$$

$$l_{mn23} = \left(D_e + D_i \right) \Delta S$$

$$l_{mn33} = \left[j\omega\varepsilon_0 \left(\Phi_e - A_e \right) + j\omega\varepsilon \left(\Phi_i - A_i \right) \right] \Delta S \qquad \text{(B.7)}$$

$$l_{mn43} = \left(j\omega\varepsilon_0 B_e + j\omega\varepsilon B_i \right) \Delta S$$

For the unknown E_{ey},

$$l_{mn14} = - \left(D_e + D_i \right) \Delta S$$

$$l_{mn24} = 0$$

$$l_{mn34} = \left(j\omega\varepsilon_0 B_e + j\omega\varepsilon B_i \right) \Delta S \qquad \text{(B.8)}$$

$$l_{mn44} = \left[j\omega\varepsilon_0 \left(\Phi_e - C_e \right) + j\omega\varepsilon \left(\Phi_i - C_i \right) \right] \Delta S$$

When m=n, corresponding to the singular points, i.e., the observation points coincide with the field points, we have the following.

A) On the conducting patch, For the unknown H_{ex},

$$
\begin{aligned}
l_{mm11} &= \int_{\Delta s} j\omega\mu \, (A_e - \Phi_e) \, dS \\
l_{mm21} &= \int_{\Delta s} - j\omega\mu \, B_e dS \\
l_{mm31} &= 0 \\
l_{mm41} &= \int_{\Delta s} D_e \, dS + 2\pi
\end{aligned}
\qquad (B.9)
$$

For the unknown H_{ey},

$$
\begin{aligned}
l_{mm12} &= \int_{\Delta s} - j\omega\mu \, B_e \, dS \\
l_{mm22} &= \int_{\Delta s} j\omega\mu \, (C_e - \Phi_e) \, dS \\
l_{mm32} &= \int_{\Delta s} - D_e \, dS - 2\pi \\
l_{mm42} &= 0
\end{aligned}
\qquad (B.10)
$$

For the unknown H_{ix},

$$
\begin{aligned}
l_{mm13} &= \int_{\Delta s} j\omega\mu \, (A_i - \Phi_i) \, dS \\
l_{mm23} &= \int_{\Delta s} - j\omega\mu \, B_i \, dS \\
l_{mm33} &= \int_{\Delta s} D_i \, dS - 2\pi \\
l_{mm43} &= 0
\end{aligned}
\qquad (B.11)
$$

For the unknown H_{iy},

$$
\begin{aligned}
l_{mm14} &= \int_{\Delta s} -j\omega\mu\, B_i \, dS \\
l_{mm24} &= \int_{\Delta s} j\omega\mu \, (C_i - \Phi_i) \, dS \\
l_{mm34} &= \int_{\Delta s} - D_i \, dS + 2\pi \\
l_{mm44} &= 0
\end{aligned}
\qquad \text{(B.12)}
$$

B) On the dielectric surface. For the unknown H_{ex},

$$
\begin{aligned}
l_{mm11} &= \int_{\Delta s} j\omega\mu \, (A_e - \Phi_e + A_i - \Phi_i) \, dS \\
l_{mm21} &= \int_{\Delta s} - j\omega\mu \, (B_e + B_i) \, dS \\
l_{mm31} &= 0 \\
l_{mm41} &= \int_{\Delta s} (D_e + D_i) \, dS
\end{aligned}
\qquad \text{(B.13)}
$$

For the unknown H_{ey},

$$
\begin{aligned}
l_{mm12} &= \int_{\Delta s} - j\omega\mu \, (B_e + B_i) \, dS \\
l_{mm22} &= \int_{\Delta s} j\omega\mu \, (C_e - \Phi_e + C_i - \Phi_i) \, dS \\
l_{mm32} &= \int_{\Delta s} - (D_e + D_i) \, dS \\
l_{mm42} &= 0
\end{aligned}
\qquad \text{(B.14)}
$$

For the unknown E_{ex},

$$
\begin{aligned}
l_{mm13} &= 0 \\
l_{mm23} &= \int_{\Delta s} (D_e + D_i) \, dS \\
l_{mm33} &= \int_{\Delta s} [j\omega\varepsilon_0 (\Phi_e - A_e) + j\omega\varepsilon (\Phi_i - A_i)] \, dS \\
l_{mm43} &= \int_{\Delta s} (j\omega\varepsilon_0 B_e + j\omega\varepsilon B_i) \, dS
\end{aligned}
\qquad \text{(B.15)}
$$

For the unknown E_{ey},

$$
\begin{aligned}
l_{mm14} &= \int_{\Delta s} - (D_e + D_i) \, dS \\
l_{mm24} &= 0 \\
l_{mm34} &= \int_{\Delta s} (j\omega\varepsilon_0 B_e + j\omega\varepsilon B_i) \, dS \\
l_{mm44} &= \int_{\Delta s} [j\omega\varepsilon_0 (\Phi_e - C_e) + j\omega\varepsilon (\Phi_i - C_i)] \, dS
\end{aligned}
\qquad \text{(B.16)}
$$

In all of the above Δs is the surface increment excluding the principal area, and the scalar Green's function in the integrals is represented by the first two terms of its Taylor series.

Appendix C

RADIATION PATTERNS OF AIR FILLED DISK PATCH ANTENNA

To investigate the effect of the ground plane size on the microstrip antenna radiation patterns, the case of a circular disk antenna is considered. This geometry was selected, since its radiation properties could be studied using existing computer programs Rot2 or Rotm [26]. Both programs are based on integral equation formulations and solve the electromagnetic field problems using the moment method. They are however useful for bodies of revolution and conductors located in free space. Using these programs we could select the size and thickness of both patch and ground plane.

The geometry of the antenna is shown in Fig.C.1, where a circular disk is located above a finite ground plane of circular shape and the diameter D. The antenna is excited by an electric dipole at the edge of the disk. Fig.C.2 and C.3 show the E and E patterns for two different diameters of the ground plane. The E patterns in Fig.C.2 are nearly the same within the range of $0 \leq \theta \leq 90^0$, i.e., above the microstrip patch. The E patterns, however, are similar only near the broadside axis and deviate rapidly beyond $\theta = 30^0$. That is, the E patterns are more sensitive to the ground plane size than the E patterns.

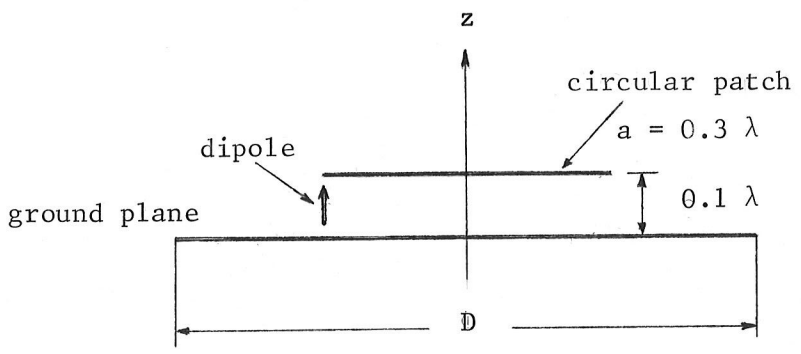

Figure C.1: The Geometry of the Disk Antenna

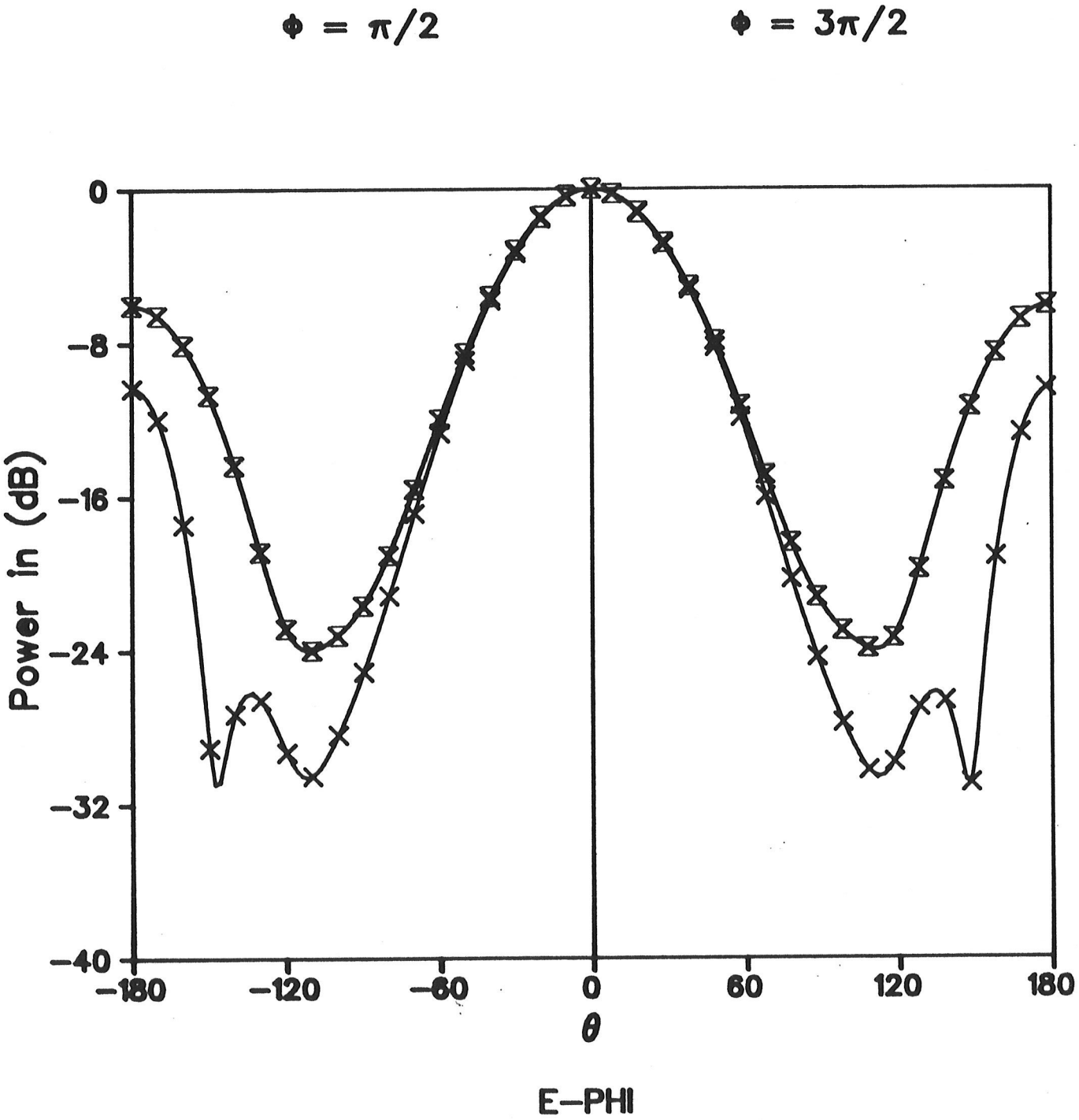

Figure C.2: × D/2 = 0.5λ DIPOLE DISTANCE = 0.3λ

⧖ D/2 = 1.0λ DIPOLE DISTANCE = 0.3λ

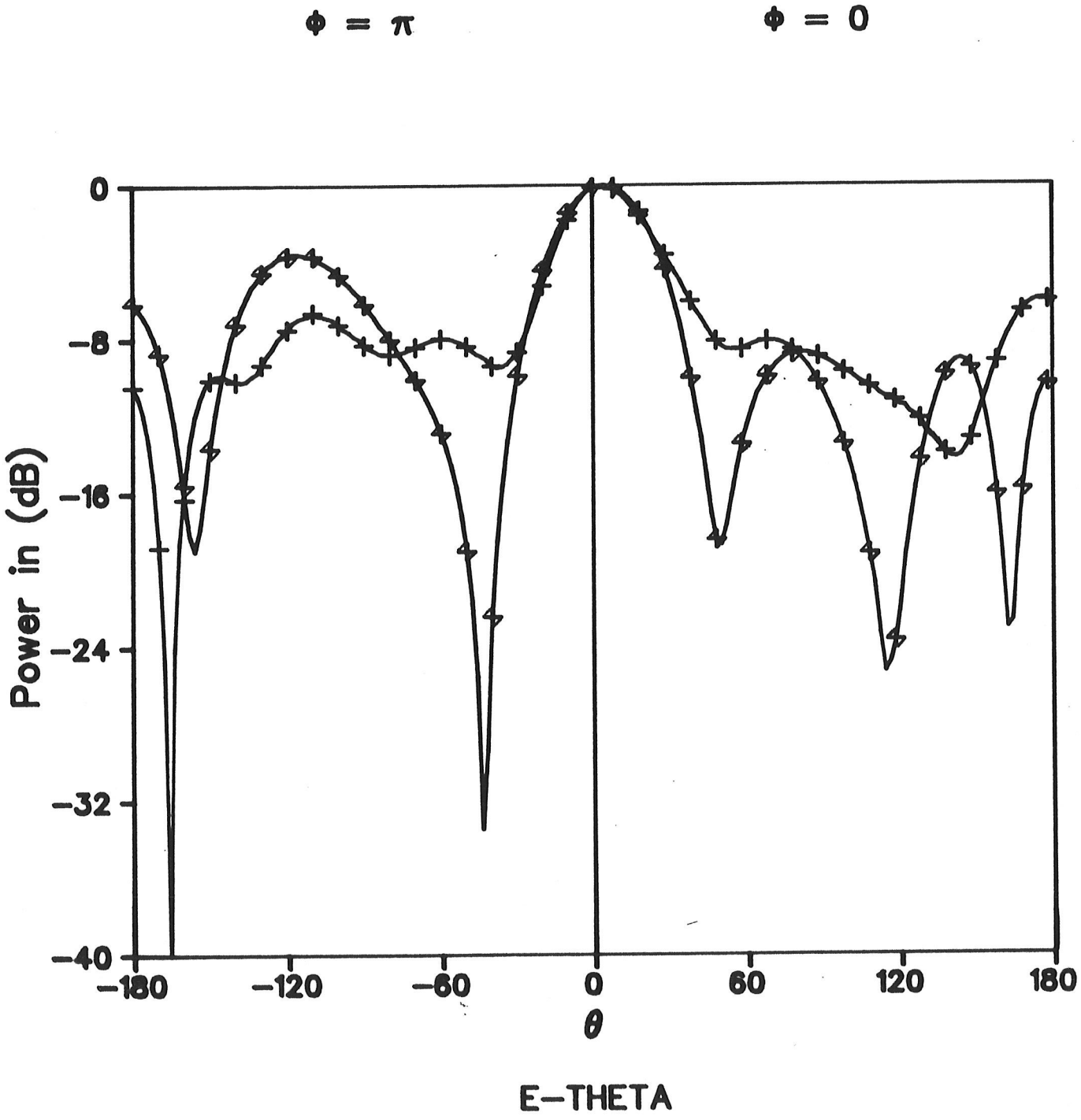

Figure C.3: + D/2 = 1.0λ DIPOLE DISTANCE = 0.3λ

4 D/2 = 0.5λ DIPOLE DISTANCE = 0.3λ

REFFERENCES

[1] A. G. Derneryd, " Linearly polarized microstrip antennas, " IEEE Trans. Antennas Propagat., vol. AP-24, pp 846-851, Nov. 1976.

[2] ----, "A theoretical investigation of the rectangular microstrip antenna element, " IEEE Trans. Antennas Propagat. vol.AP-26, pp. 532-533, July 1978

[3] P. K. Agrawal and M. Bailey, " An analysis for microstrip antennas, " IEEE Trans. Antennas Propagat. vol. AP-25, pp 756-759 Nov. 1977

[4] Y. T. Lo, D. Solomon, and W. F. Richards, "Theory and experiment on microstrip antennas, " IEEE Trans. Antennas Propagat. AP-27, pp 137-145 Mar. 1979

[5] S. A. long, L. C. Shen and P. B. Morel, "Theory of the circular-disc printed-circuit antenna, " Proc IEEE vol. 126, No.10 pp 925-928, Oct. 1978

[6] W. C. Chew and J. A. Kong, " Radiation characteritics of a circular microstrip antenna, " J. Appl. Phys. 51(7), pp 3907-3915, July 1980

[7] K.R.Carver and E.L.Coffey, "Theoretical investigation of the microstrip antenna, " Physic. and Sci. Lab., New Mexico State Univ., Las Cruces, Tech.Rep.PT-00929, Jan. 23, 1979

[8] J. R. James and G. J. Wilson, "Microstrip Antenna and

Array. Pt.1-Fundamental action and limitations," IEE. J Microwaves, Opt. & Acoust., 1977, 1, pp 165-174

[9] K. R. Carver and J. W. Mink, "Microstrip Antenna Technology, " IEEE Trans. Antennas Propagat. Vol. AP-29, pp 1-37 Jan. 1981

[10] E. H. Newman and P. T. Tulyathan, " Analysis of microstrip antennas using moment method," IEEE Trans. Antennas Propagat. vol. Ap-29 pp 47-53 Jan. 1981

[11] S. L. Chuang, L. Tsang, J. A. Kong and W. C. Chew, The Equivalence of the Electric and Magnetic Current Approaches in Microstrip Antenna Studies, " IEEE. Trans. Antennas Propagat. Vol. AP-28 pp 569-570

[12] M. C. Bailey and M. D. Deshpande "Integral Equation Formulation of Microstrip Antennas, " IEEE Trans. Antennas Propagat. vol. AP-30, pp 651-656, July 1982

[13] R. H. Harrington, " Time-Harmonic Electromagnetic Field, " Mcgraw-Hill Book Co., New York, 1961

[14] R. Mitra, "Computer Techniques for Electromagnetics," Pergamon Press, P.162-164 and 167-170

[15] A. D.Yaghjian, "Augmented electric- and magnetic-field integral equations, " Radio Science Vol.16, pp Nov.-Dec. 1980

[16] V . J . Blade/ " Electromagnetic Fields, " 556 pp., Mcgraw-Hill, New York, 1964

[17] G. Strang and G. J. Fix, "An Analysis of the Finite Element Method, " pp.70-71, Prentice-Hall, Englewood 1973

[18] R.H.Harrington,"Field Computation by Moment Methods," Macmillian Co., New York, 1968

[19] P. Hammer, D.Van. Bouchaute, D. Verschaeven and A.Van Don Chapelle, " A Model for Calculating the Radiation Field of Microstirp Antennas, " IEEE Trans. Anttenas Propagat. vol. AP-27 pp.267-269, March 1977

[20] I. J. Bahl and P. Bhartia, " Microstrip Antennas, " pp. 17-18, Artec House, Massachusetts, 1980

[21] J. R. James and A. Henderson, " High-frequency behaviour of microstrip open-circuit terminations, " IEE. J. Microwaves, Opt. & Acoust., 1979, 3, pp 205-218

[22] J.R. Mautz and R.F. Harrington " Boundary Formulations for Aperture Coupling Problems, " pp.377-384 AEU.Band 34 [1980]. Heft 9

[23] A. A. MOHSEN " On the Integral Representation of Electromagnetic Field Vectors, " IEEE Trans. Antennas. Propagat. Vol. AP-29, pp 148-153 Jan. 1981

[24] David M. Pozar, " Input Impedance and Mutual Coupling of Rectangular Microstrip Antennas, " IEEE Trans. Antennas. Propagat. Vol.AP-30, pp 1191-1196, Nov. 1982

[25] E. Lier " Improved Formulas for Input Impedance of Coax-fed Microstrip Antennas, " IEE J Microwave, Opt. Acoust., 1982, 8, pp 161-164

[26] K. A. Iskander, L. Shafai, A. Frandsen and J.E. Hansen "Application of Impedance Boundary Conditions to numerical Solution of Corrugated Circular Horns " Trans. Antennas. Propagat. Vol. AP-30, pp 366-372 May 1982